Study of DXA-derived Cortical Bone Thickness in Assessing Hip Fracture Risk

By

Yujia Long

A thesis submitted to
the Faculty of Graduate Studies
in partial fulfilment of
the requirements for the degree of
Master of Science

Department of Mechanical Engineering
Faculty of Engineering
University of Manitoba
Winnipeg, Manitoba

July 2014

Abstract

Hip fracture has been identified as one of the main health problems in the elderly. To improve the accuracy in assessing subject-specific hip fracture risk, this study proposed normalized cortical bone thickness (NCBT) estimated from patient's hip DXA as an alternative predictor of hip fracture risk. Hip fracture risk index (HFRI) derived from DXA-based finite element model was utilized as a baseline for evaluating the effectiveness of NCBT in predicting hip fracture risk. It was found that NCBT at the lateral side of the narrowest femoral neck had the strongest correlation with femoral neck HFRI among the six locations of the proximal femur. This study suggests that it is possible to use NCBT as a surrogate for a quick evaluation of hip fracture risk. Yet its clinical performances such as sensitivity to therapy effectiveness and the ability to discriminate clinical fracture cases will be investigated in a future study.

Acknowledgments

I owe gratitude to a number of people. First, I would like to thank my supervisor, Dr. Yunhua Luo, for offering me the opportunity to study in Canada and participate in this project, and for his motivating guidance and support throughout the research work and the completion of my dissertation.

I want to thank the Manitoba Bone Mineral Density Database and the Winnipeg Health Sciences Center for providing the clinical cases in this study.

I would also like to thank my colleagues Siamak, Masoud, Eniyavan, Heng, Qingguo, Hossein, and Ida in the Computational Biomechanics Group for their discussions. I am really grateful to all the friends I made in Canada for mutual support and encouragement to overcome all the challenges I went through during this two-year study.

Above all, I am deeply indebted to my parents, grandparents, uncles, aunts, and cousins for their unconditional love throughout my life. You have been instilling faith and courage into my soul and body, which are the two key elements that orient me on the right way to succeed in the future.

Contents

List of Tables

List of Figures

List of Copyrighted Material

Figure 2-1 was cited from Wikipedia. Permission was obtained on May 22nd, 2014.

Figure 3-1 was cited from Advanced Orthopedic Specialists. The permission was obtained on May 23rd, 2014.

List of Abbreviations

aBMD	areal Bone Mineral Density
BIT	Bone Investigation Toolkit
BMC	Bone Mineral Content
BMD	Bone Mineral Density
BMI	Body Mass Index
CBT	Cortical Bone Thickness
CT	Computed Tomography
CTXA	Computed Tomography X-ray Absorptiometry
CV	Coefficient of Variation
DXA	Dual-energy X-ray Absorptiometry
FEA	Finite Element Analysis
FEM	Finite Element Model
FNA	Femoral Neck Axis
FNAL	Femoral Neck Axis Length
FNSA	Femoral Neck-Shaft Angle
FSA	Femoral Shaft Axis
FRAX®	Fracture Risk Assessment Tool
HFRI	Hip Fracture Risk Index

HSA	Hip Structural Analysis
HU	Hounsfield Unit
IT	Intertrochanter
MRI	Magnetic Resonance Imaging
NCBT	Normalized Cortical Bone Thickness
NFN	Narrowest Femoral Neck
QCT	Quantitative Computed Tomography
ROI	Region of Interest
FS	Femoral Shaft
SD	Standard Deviation
3-D	Three Dimensional
2-D	Two Dimensional
vBMD	volumetric Bone Mineral Density
WHO	World Health Organization

List of Symbols

r_1	Endosteal width of narrowest femoral neck
r_2	Periosteal width of narrowest femoral neck
r_3	Endosteal width of femoral shaft cross-section
r_4	Periosteal width of femoral shaft cross-section
a_1 and b_1	Endosteal widths of intertrochanter cross-section
a_2 and b_2	Periosteal widths of intertrochanter cross-section
a	Centroid of narrowest femoral neck
A	Centroid of intertrochanter cross-section
m	Bone mass
ρ_1	Density of trabecular bone
ρ_2	Density of cortical bone
y'	Distance traversing width of hip bone
$\boldsymbol{D}$	Material matrix
E	Young's modulus
υ	Poisson's ratio
ρ_a	Areal bone mineral density
F	Fall force
h	Body height of the subject

w	Body weight of the subject
σ_{VM}	von Mises stress
σ_x	Nodal or Gaussian point's stress at x-direction
σ_y	Nodal or Gaussian point's stress at y-direction
τ_{xy}	Nodal or Gaussian point's stress at xy-plane
σ_Y	Yield stress
η_{ROI}	Hip fracture risk index over an ROI
A_i	Area of finite element i
p	Probability of statistical significance
r^2	Coefficient of determination
n	Number of the measured cases
$x_j^{(1)}$ and $x_j^{(2)}$	Initial and follow-up measurement for subject j
$\bar{x}_j$	Mean of the measurements for subject j
$\bar{e}$	Average relative error

Chapter 1

Introduction

1.1 Motivation and Background

Hip fractures lead to long-term disability, a lower quality of life, and in more than 15% of cases fatality [1-5]. A survey of women aged 75 years and up revealed that 80% of respondents would choose to be dead than suffer the loss of independence and the decreased quality of life stemming from hip fractures [6]. Actually, most hip fractures are attributed to osteoporosis and falls, which were responsible for approximately 1.66 million hip fractures worldwide in 1990 [3]. With the aging population, the number of acute hip fractures is projected to grow to an alarming 6.26 million worldwide in 2050 [3]. Furthermore, the high cost of medical care associated with osteoporotic hip fractures is becoming a burden to the society. For example, in the United States alone, $12.2 billion was spent on hip-fracture-related hospitalization and nursing home services in 2005 [2]. In Canada, the total direct costs associated with osteoporotic hip fractures are projected to be $2.4 billion by 2041 [7]. Tools such as hip DXA (dual-energy X-ray absorptiometry)

and FRAX® (fracture risk assessment tool) have been adopted by the World Health Organization (WHO) for evaluating hip fracture risk.

The areal bone mineral density (aBMD) measured by DXA is currently the gold standard proposed by the WHO to screen osteoporosis and assess hip fracture risk [8, 9]. A clear diagnostic criterion for osteoporosis has been defined by the WHO which will be described later in this thesis. FRAX® is a computer-based algorithm which integrates clinical hip fracture risk factors in assessing fracture probability in men and women [10, 11]. This tool can be utilized together with femoral neck aBMD to enhance the prediction of 10-year fracture probability [11]. Both aBMD and FRAX® are dependent on the statistical models established by large cohort studies [10, 12]. Therefore, deficiencies appeared in predicting hip fracture risk. Although it is effective in predicting trends in hip fracture risk in a large population, DXA-derived BMD is limited for identifying fracture in individuals, as subjects with or without hip fractures may have the same BMD values [12]. Moreover, when utilizing FRAX®, many countries do not have the necessary data to construct their own FRAX® model [13] which impedes its application worldwide.

Apart from the above WHO-defined tools, finite element analysis (FEA) is currently the most popular methodology for evaluating bone strength in the field of orthopaedics. With state-of-the-art computing facilities and computational methods, the reliability and validity of assessing hip fracture risk by the finite element model (FEM) has been greatly improved and well demonstrated [14-18]. However, FEA has not been adopted into clinical environment due to its technical complexity and the uncertainties in the kinematic and kinetic conditions of the subject involved in an accident.

The limitations of the aforementioned methods in evaluating hip fracture risk suggest development of a better predictor. We considered cortical bone thickness (CBT) can accurately assess hip fracture risk based on previously reported research [19-22]. These studies have demonstrated that CBTs at the femoral neck and/or femoral shaft can be identified as the predictors for hip fracture risk independently of BMD [19-22]. A number of algorithms have been implemented to measure CBT in the proximal femur from quantitative computed tomography (QCT) image [19, 20, 23, 24]. However, their ability to measure CBT is limited since the thickness of cortex may be overestimated due to the limited spatial resolution [23, 24], but also because of the concern of relatively high radiation exposure in QCT scanning which might cause health problems [25]. Several studies have been implemented to measure average cortical thickness from DXA image [26-28], but all of them employed certain assumptions on the shape of the proximal femur resulting in an equivalent rather than real CBT. On the other hand, few studies reported medial and lateral CBT derived from DXA image; these thicknesses are crucial in determining hip fracture risk as presented in the previous studies [29-31].

For the above reasons, this thesis introduces an algorithm to measure CBT from DXA image at the three critical cross-sections of the proximal femur, namely, the narrowest femoral neck (NFN), the intertrochanter (IT) cross-section, and the femoral shaft (FS) cross-section. To integrate hip geometric parameters and individual differences such as body weight and height, a new parameter known as normalized cortical bone thickness (NCBT) is developed. It is assumed that a stronger correlation between NCBT and hip fracture risk index (HFRI) derived from the DXA-based finite element model [32, 33] would imply NCBT can be a surrogate of HFRI in assessing hip fracture risk in this study.

1.2 Objective of the Reported Research

The objective of this dissertation is to find a surrogate of HFRI which can be used by clinicians as a quicker predictor for assessing hip fracture risk. A total of 210 clinical cases were obtained from the Manitoba Bone Mineral Density Database for this investigation. For each clinical case, NCBTs at the six locations of the proximal femur are estimated from DXA image by the in-house MATLAB codes developed in this study. Furthermore, HFRI derived from the DXA-based finite element model is used as a baseline for evaluating the effectiveness of NCBT in assessing hip fracture risk. Correlations between the studied variables are examined by linear regression analysis using SPSS software (IBM SPSS 22, New York, USA) to determine NCBT can substitute HFRI in assessing hip fracture risk in this study.

1.3 Outline of the Reported Research

This thesis is organized in the following manner:

Chapter 2 - In this chapter, the bone structure of human femur will be illustrated. Furthermore, structural and material behavior of a whole bone followed by the mechanical properties of cortical and trabecular bone will be introduced. Finally, factors affecting age-related bone loss and bone disease such as osteoporosis will be described.

Chapter 3 - In this chapter, types of hip fractures will be classified. Then, currently available methods for predicting hip fracture risk, including BMD extracted by medical imaging, FRAX®, proximal femur geometry, and finite element analysis, will be reviewed with respect to their strengths and limitations in clinical applications.

Chapter 4 - In this chapter, a new predictor known as NCBT will be introduced. Enrollment of cases and the algorithm of estimating CBTs and other hip geometric parameters from DXA images will be developed. The procedure of validation of DXA-derived CBT will be presented. Short-term precision study will be introduced.

Chapter 5 - In this chapter, the procedure of constructing a DXA-based finite element model of the proximal femur will be explained step by step. HFRI derived from this finite element model at pre-defined regions of the proximal femur will be used as the baseline for assessing hip fracture risk. Verification of DXA-based finite element model will be provided.

Chapter 6 - In this chapter, validation and verification results will be provided and explained to show the high accuracy of the in-house developed MATLAB codes. Convergence tests of HFRIs derived from the in-house developed MATLAB codes will be presented. Furthermore, correlation analyses between the studied variables will be examined to demonstrate the validity and acceptability of the new predictor. Short-term precision studies on NCBT and HFRI will be presented to show the extent of repeatability.

Chapter 7 - In this chapter, implications of the results derived from the validation and verification of the in-house developed MATLAB codes, convergence tests, correlation analyses, and short-term precision studies will be discussed.

Chapter 8 - In this chapter, major conclusions and contributions will be drawn from this reported research. Future research will be presented to reduce the limitations of current research along with the extent of possibilities for exploiting the new predictor.

Chapter 2

Structure and Physiology of Bone

The skeletal system is composed of bones and joints in vertebrate body. The main functions of bone include supporting body structure, protecting soft tissue and internal organs, being a lever for muscles to move at the joints, acting as a storehouse for fat and minerals, and generating blood cells. Bone is a dynamic material which meets the required mechanical demands via bone modeling and remodeling, altering morphology and tissue properties.

2.1 Bone Structure

Bone has a very complex structure made up of 70% mineral (calcium phosphate hydroxyapatite in the form of tablet-, rod-, and needlelike crystallite), 22% to 25% organic matrix (90% collagen fibrils and only 10% noncollagenous proteins), and 5% to 8% water and cells (osteoblasts, bone-lining cells, osteocytes, and osteoclasts) [34, 35]. Generally, these compositions of bone contribute to stiff but tough properties that maintain the shape of human body [36].

Depending on the anatomic sites and shapes, bone can be classified into long (e.g. humerus, tibia and femur), flat (e.g. skull and rib), short (e.g. carpus and tarsus) and irregular (e.g. vertebrae and mandible) bone. Typically, a long bone is composed of a long cylindrical shaft (diaphysis) and two extreme and rounded parts (epiphyses); the metaphysis connects the diaphysis with the epiphysis (Figure 2-1). In spite of the macroscopic anatomy, all the bones possess an outer layer of cortical or compact bone and the inner space of trabecular or spongy bone (Figure 2-1). The diaphysis of a lone bone, for example, has a thick cortical bone shell while the medulla which is surrounded by cortical bone consists mainly of trabecular bone [37]. In fact, proportions and distributions of cortical and trabecular bone vary with the skeletal sites, but the maximum strength-to-weight ratio keeps its validity in their normal functions [34].

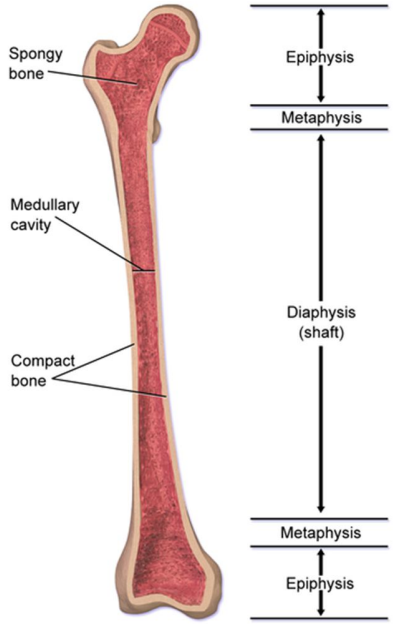

Figure 2-1 Structure of a quintessential lone bone (human femur) [38] (courtesy of Wikipedia)

2.2 Mechanical Properties of Bone

From an engineering perspective, bone is an anisotropic and inhomogeneous material. Mechanical properties of bone therefore can be described by load-deformation relation at the structural level and stress-strain relation at the material level. The load-deformation curve (Figure 2-2) represents the deformation of the specimen (whole bone) in response to the load applied on it. The slope of the elastic region represents the extrinsic stiffness of bone structure. Additionally, other biomechanical properties can also be extracted from this curve. For example, after a yield point, the bone specimen undergoes a permanent plastic deformation. The failure point corresponds to the ultimate load (failure load) and the ultimate displacement. The area under the load-deformation curve is the amount of energy absorbed by the bone specimen prior to the bone failure or fracture.

Normalized load known as stress (force per unit area) and normalized deformation known as strain (geometric change in a material) are intrinsic material properties of bone and therefore, the stress-strain curve is analogous to the load-deformation one (Figure 2-2).

The strength of cortical bone is higher than that of trabecular bone at both the structural and material levels, but their mechanical properties vary with the types of mechanical testing [34]. It has been examined that both cortical and trabecular bones have larger strength and elastic modulus in compression than tension whereas the torsion or shear is the weakest in both the structural and material (tissue) levels [34].

The mechanical properties of cortical and trabecular bone are anisotropic, i.e., their mechanical properties depend on the direction of the applied load. Both of them have the highest strength and elastic modulus in the longitudinal direction (0º approximately weig-

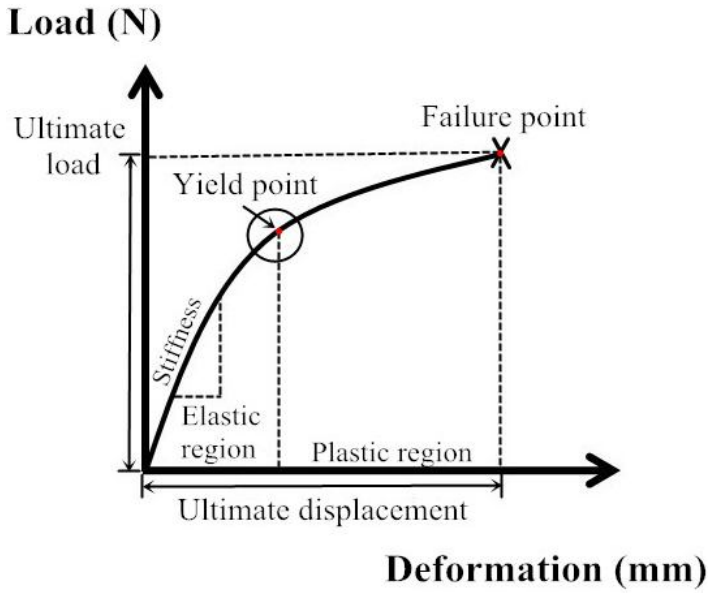

Figure 2-2 A typical load-deformation curve from mechanical testing of a bone specimen

ht-bearing direction), lowest strength and elastic modulus in the transverse plane (90º lateral direction perpendicular to longitudinal axis), and intermediate values in any angles between 0º and 90º [39, 40]. While the underlying mechanism of anisotropy for trabecular bone is not well understood, arrangement of the osteons is accountable for the anisotropic characteristic of cortical bone [34]. The mechanical properties of cortical bone are mostly dependent on the porosity and the degree of mineralization [41]. Currey found that these two variables explained more than 80% of the stiffness variation [41]. When the porosity is increased from 5% to 30%, both elastic modulus and ultimate stress of cortical bone can be decreased by 50% [42], which reveals the porosity has a strong effect on the mechanical properties of cortical bone. On the other hand, apparent density is the most important determinant in the mechanical properties of trabecular bone, as evidenced by the empirical functions established from experiments [43, 44]. Hernandez et al. found that the power-law relationships with regard to the apparent density can explain 60% to 90% variation in the elastic modulus and the strength of trabecular bone [43].

2.3 Age-related Bone Loss and Osteoporosis

Human bone mass increases during growth, peaks in young adults, and decreases after 30 years old or so [45]. With age advances, bone is lost in all skeletal sites under different rate. A number of factors influence age-related bone loss, for example, estrogen deficiency [46], less intake of calcium and vitamin D [47], and lack of physical activity [48]. The cessation of estrogen production after menopause increases the life expectancy of osteoclasts, thus breaking the balance of bone remodeling. Therefore, more bone is resorbed than is formed. Decrease in calcium and vitamin D has major impacts on bone strength. Without sufficient calcium and vitamin D absorption in the body, both calcium homeostasis and bone remodeling are broken, leading in general to the onset of bone disease such as osteoporosis. Physical exercise has significant impacts on adolescents, maximizes peak bone mass in young adults, reduces age-related bone loss, and maintains or even enhances muscle power. Hence, proper life-long physical exercise is recommended in order to maintain bone mass and bone quality.

Due to age-related bone loss, the adverse outcome such as osteopenia or even osteoporosis may occur. Osteoporosis is a skeletal disease characterized by a decrease in bone mass and deterioration in bone microarchitecture with a consequential increase in bone fragility and fracture risk [36]. A patient with osteoporosis normally has the same bone composition of a healthy person, but cortical bone becomes thinner and trabecular bone is more porous. The underlying causation of osteoporosis is a disrupted balance between bone resorption and formation; usually either bone resorption exceeds bone formation or bone resorption lags behind bone formation, or both occur simultaneously. Therefore, under-

standing the mechanism of bone modeling and remodeling is essential to investigate the pathogenesis of osteoporosis.

Osteoporosis has been defined on the basis of BMD measurement. According to the criteria of the WHO, osteoporosis is defined as a BMD value that lies 2.5 standard deviation (SD) or more below the young mean value (T-score = -2.5 SD) [8]. If a T-score is below 2.5 SD along with one or more fragility fractures, this condition is defined as severe osteoporosis. Although this approach to defining osteoporosis has low sensitivity, the high specificity and the proper cut-off values for osteoporosis help doctors develop effective interventions and remedies for the patients.

Chapter 3

Hip Fracture and Risk Assessment

Clinically, osteoporotic fractures are usually caused by a low trauma such as a fall from standing height. They generally include vertebral fractures, distal forearm fractures, and hip fractures [9]. These fractures have posed major public health concern to the whole world. Among these types of osteoporotic fractures, hip or proximal femur fractures are the most severe ones [4]. Although many studies have shown that there is a close correlation between the frequency of osteoporotic hip fractures and older age, accident falls precede most hip fractures [3, 4]. Therefore, in order to study the etiology of hip fractures, the above two factors, namely, the applied loads to bone and bone strength, should be considered.

3.1 Hip Fracture Types

Generally, hip fractures can be classified into three types, i.e., cervical (femoral neck) fractures, intertrochanteric fractures, and subtrochanteric fractures. Cervical fractures occur at the neck or the head of the femur and are typically within the capsule, whereas in-

tertrochanteric and subtrochanteric fractures occur between the neck of the femur and lesser trochanter, and below the lesser trochanter respectively [49].

Cervical fractures are one of the common injuries in the elderly, especially in the women. These fractures occur within the capsule and can be further subdivided into subcapital and transcervical fractures (Figure 3-1). It is recommended to do surgical operation (hip replacement) if this kind of fracture occurs since the process of healing may be disrupted by the reduced blood supply to the femoral head, which may lead to complications such as femoral head necrosis. However, for a cervical fracture with small or no displacement, fixation of fracture site and protection of femoral head can be applied to treat the fracture.

The epidemiology of intertrochanteric fractures is similar to that of cervical fractures and this type of fracture is common in women as well. Since the blood flow is usually not blocked by this kind of fracture, it can be treated with traditional surgical methods using a metal plate and screws. However, the treatments of these fractures are relatively complex compared with the cervical ones due to the considerable forces induced by the attached muscles. Therefore, the skills and experience of orthopedic surgeons are very important.

Subtrochanteric or femoral shaft fractures are not as common as cervical and intertrochanteric fractures, but are more difficult to fix due to its instability arising from the high stresses during daily activities. In addition, the subtrochanter is subject to torsional effects induced by the attached muscles which give rise to rotational shear forces. Hence, the above factors lead to this kind of fracture hard to consolidate and heal.

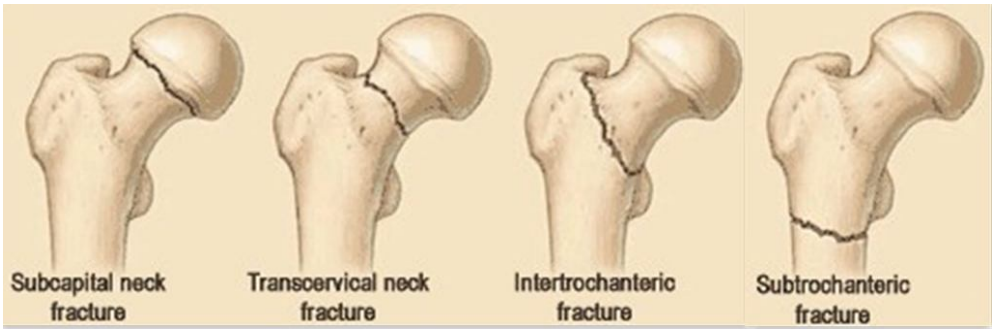

Figure 3-1 Three main types of hip fractures: cervical fractures (subcapital and transcervical fractures), intertrochanteric fractures, and subtrochanteric fractures [50] (courtesy of Advanced Orthopedic Specialists)

3.2 Methods for Evaluating Hip Fracture Risk

3.2.1 BMD Extracted by Medical Imaging

At present, common methods for measuring BMD are DXA and QCT. DXA employs two different X-ray energies to determine bone mineral content (BMC). With the preselected area, aBMD (in g/cm^2) can be derived via BMC divided by the region of interest (ROI) on lumbar spine, hip, forearm, or even whole body. The aBMD of an individual is then compared to the references in a proper population database, and the result is commonly expressed as T-score and Z-score. The T-score of a specific patient is the standard deviation above or below the mean value in young female [9]. The operational range of T-score for diagnosing osteoporosis has been recommended by the WHO and shown in Table 3-1. However, the limitation of using T-score lies in subjects with or without hip fractures may have the same BMD values [12]. Z-score, an indicator comparing the patient's aBMD with the mean value derived from the same age, sex, and ethnicity, is sometimes used in assessing hip fracture risk [52]. However, its use may be confusing si-

Table 3-1 Criteria of the WHO for defining normal, osteopenia, osteoporosis, and severe osteoporosis

T-score	Diagnosis
Above -1	Normal
-1 to -2.49	Osteopenia
≤ -2.5	Osteoporosis
≤ -2.5 with fragility fractures	Severe osteoporosis

nce it obscures age as a risk factor in assessing osteoporosis [51].

QCT is a well-established medical technique that measures volumetric bone mineral density (vBMD) in lumbar spine, hip, and forearm using a standard phantom that contains materials representing the liquid-like and bone-like contents for density calibration. In contrast to planar DXA scan which is widely utilized currently, information such as three-dimensional (3-D) geometry and vBMD (in mg/cm^3) of cortical and trabecular bone is accessible from QCT [53]. However, the costs and ionising radiation exposures are higher in QCT than in DXA. Moreover, the criteria of diagnosing osteoporosis based on DXA-derived aBMD may not be applicable to QCT-derived vBMD. In spite of these drawbacks, technicians can acquire 3-D images more rapidly and obtain the structures of cortical and trabecular bone more accurately with technical developments in QCT [53]. A 3-D finite element model with higher biofidelity can be constructed as well using QCT image [53].

Magnetic resonance imaging (MRI) is a recently developed radiology technique to evaluate hip fracture risk without exposing to high X-ray radiation. Compared with QCT, not only MRI-derived BMD can be obtained [54], but also in vivo imaging of bone quality such as bone tissue properties and microstructure using MRI may be more effective for determining bone strength [55]. However, MRI devices are more difficult to operate and

the equipment is not as commonly accessible as DXA or QCT scanners due to its high cost of production.

3.2.2 FRAX®

FRAX® was introduced by the WHO in 2008 in order to evaluate an individual's fracture probability in the next 10 years and provide clinical guideline for pharmacological intervention. The probability is produced on the basis of the involved clinical risk factors with or without aBMD at the femoral neck. The clinical risk factors include body mass index (BMI), a prior history of fracture, a parental history of hip fracture, use of oral glucocorticoids, rheumatoid arthritis and other secondary causes of osteoporosis, current smoking, and alcohol intake 3 or more units per day [10]. It should be noted that fracture probability varies appreciably among different zones of the world, which may complicate using this model for determining intervention threshold for the fracture probabilities [56]. Although this computer-based tool has been validated in several studies [10, 57], some countries have insufficient data for developing this model [56] and thus, these countries have to choose their surrogates based on the categories of hip fracture likelihood, which may bring inaccuracy to prediction.

3.2.3 Proximal Femur Geometry

A majority of studies have reported that the non-invasive evaluation of proximal femur geometry using DXA or QCT is capable of predicting hip fracture risk, but it is still uncertain whether these geometric measures can improve hip fracture prediction independent of or even better than BMD measurements [58-65]. Femoral neck width, femoral

neck area, and femoral neck axis length are found to be correlated positively with femur strength [61, 63], whereas other researchers observed that increased femoral neck width, femoral neck axis length, and femoral neck-shaft angle were negatively correlated with femur strength [58, 59, 64, 65]. To our best knowledge, the longer the femoral neck axis length, the larger the bending moment the femoral neck will have to withstand in a fall, which should result in higher hip fracture risk. The contradictory observation that femoral neck axis length had a positive correlation with femur strength in the in vitro experiments might be because of changed materials and physiological conditions in the cadaveric femora [66]. Plastic mechanical properties may be significantly different in the non-fresh cadaveric femora which may affect the measurements of failure loads [66]. Furthermore, the change of femoral neck width associating with femur strength are controversial [67]. The width of femoral neck increases with age in order to compensate for the gradual decrease in bone strength due to age-related bone loss [28, 67]. However, femur widening may not be adequate to resist different types of hip fractures, and thus different conclusions have drawn. In considering the influence of femoral neck-shaft angle, hip fracture risk may be related to the direction of force because, theoretically, a wider femoral neck-shaft angle decreases the stress occurring in the femoral head in stance, while it increases the stress in a lateral fall.

Hip structural analysis (HSA) incorporates the relevant structural parameters such as section modulus, cross-sectional moment of inertia, mean cortical thickness, and buckling ratio estimated from DXA scans in assessing femur strength [68]. All the above variables can be calculated in vivo using the HSA software [68]. The principle of measuring the strength-related structural dimensions is that a line of X-ray beams traverse the bone

width at that location, constituting the projection of that cross-section [68]. Although HSA considers both aBMD and geometric strength, it is not very helpful to clinicians due to its much lower precision compared with the traditional aBMD, in particular for the thin bones in osteoporotic patients [69]. Furthermore, DXA scanners have not been designed for geometry measurement. A number of factors such as noise, resolution and positioning may affect the projected contour of the proximal femur [69, 70]. A few studies have demonstrated that HSA-derived parameters are not superior to aBMD in predicting hip fracture risk [26, 58]. This may arise from the deficiency of applying a beam model where a plane cross-section remains planar after deformation, which may be invalid for the femur bone. As the deformation of femur bone is very complex, particularly in the region of femoral neck and intertrochanter where osteoporotic fractures occur frequently, this assumption is over-simplified and cannot be utilized to assess hip fracture risk.

Cortical bone is the main compartment for the femur to resist fracture [19-21, 67, 71, 72]. Most research utilized the HSA-derived average cortical thicknesses to study hip fracture risk [26-28]. They found that the estimated average cortical thicknesses were significantly lower in the fractured cases compared with the controls [26-28]. However, as this parameter is predicated on the assumptions of constant bone tissue mineralization and regular bone shape, the estimation is not accurate for an individual patient. In effect, thinner cortex has been reported as a risk factor for hip fracture [29, 67, 73]. Rivadeneira et al. have reported that the superior or lateral cortices are thinner than the inferior or medial ones at the narrowest femoral neck; the thin superior cortices can serve to predict hip fracture risk, especially in the prediction of local buckling [67]. As age advances, significantly thinning of cortices at the superior side of the femoral neck will occur [73]. In a

sideway fall, the impact force is applied onto the greater trochanter, and the maximal compressive strain occurs at the superior side of the femoral neck [29]. Therefore, the role of cortical bone thickness in predicting hip fracture risk will be further explored in this study.

3.2.4 Finite Element Method

Finite element analysis was introduced in early 1970s to assess stresses in human bones in the field of orthopedic biomechanics [74], which is now becoming a very helpful tool in orthopedics and other biomedical engineering fields. From the viewpoint of biomechanics, bone fracture is determined by three sets of factors: bone material properties, bone geometry, and loading/boundary conditions. Conventional aBMD or T-score only estimates the first of the three sets of factors and thus is not adequate to assess femur strength. As yet, hip geometric parameters have not demonstrated their superiority to BMD in predicting hip fracture risk, as demonstrated by a large scale evaluation using over 30,000 women cases from the Manitoba Bone Mineral Density Database [58]. FE model of the proximal femur has the potential to increase the accuracy in assessing hip fracture risk compared with currently available method like aBMD [16, 17, 75-77]. In effect, it has been found that two-dimensional (2-D) and 3-D models constructed from medical images such as DXA and QCT can be used for predicting fracture load or femur strength [14, 16-18, 75-78]. For the FE simulations, FE software such as ANSYS, ABAQUS, BONEMAT or in-house developed codes can be used. In this section, relevant studies and their findings in assessing hip fracture risk using FEA will be discussed.

Testi et al. developed a 2-D finite element model of the proximal femur from DXA image in predicting hip fracture risk and their simulated results were validated in vitro with the femur replica [78]. Their results were also compared with a 3-D finite element model. A good agreement was found between these two models. Although they simulated a sideways fall onto the greater trochanter, a constant impact force was utilized in their study, which cannot reflect the effects of individual body weights and heights. Another major limitation of their study was that a linear correlation between bone density and bone material properties was used, which was not consistent with the power law established in the experiments [44].

Cody et al. used DXA, QCT, and FE models to predict femur strength in vitro [17]. The statistical models for predicting femur strength were developed by the regional bone density and structures derived from DXA and QCT. The QCT data were utilized to construct a 3-D finite element model to predict femur strength as well. Although their findings showed that FE models predicted femur strength better than the statistical models constructed from DXA and QCT, only a stance loading configuration was used in their FE models, which may not adequately reflect the hip fracture mechanism since hip fracture usually occurs during a fall.

Koivumaki et al. proposed a CT-based nonlinear finite element models to estimate experimentally measured fracture loads in the proximal femur in vitro [16]. The geometric models of the proximal femurs were segmented by Mimics and trabecular and cortical bone was modeled separately. A group of femora was used to establish the strain threshold for the element failure criteria while another group was used to validate the accuracy in estimating the experimentally measured failure loads. A sideways fall was applied on

the greater trochanter and the bottom end of the proximal femur was completely fixed in order to simulate the experimental setup. Although a high correlation between simulated fracture loads and experimental data was found ($r = 0.931$, $p<0.001$), the average computation time to solve the FE models was more than several hours, indicating that it was a time-consuming process and cannot be used in the clinical environment.

Luo et al. proposed a DXA-based subject-specific finite element model for assessing osteoporotic hip fracture risk [33]. HFRIs were created based on the three types of hip fractures which have been discussed in Section 3.1. The larger the HFRIs, the more likely the patients will experience hip fractures. Since these three HFRIs are defined based on the three critical cross-sections, they are very sensitive to the selected cross-sections and thus have lower repeatability. Therefore, an ROI-based HFRI was introduced in [32]. This averaging operation can not only improve the precision of HFRI, but also be consistent with the conventional aBMD which is currently used in the clinical environment.

Chapter 4

Derivation of Cortical Bone Thickness from DXA

4.1 Introduction of Normalized Cortical Bone Thickness

Current methods for evaluating hip fracture risk are limited, suggesting development of an improved predictor. We assume that cortical bone thickness in the proximal femur has the potential to be an alternative predictor to enhance the prediction of hip fracture risk based on the reviews of Chapter 3. Nevertheless, in order to incorporate aBMD, proximal femur geometry, body weight, and body height from a specific subject, a novel parameter known as normalized cortical bone thickness (NCBT) is proposed as follows:

$$NCBT = \frac{(cortical\ bone\ thickness)\times(areal\ bone\ mineral\ density)}{(femoral\ neck\ axis\ length)\times(femoral\ neck{-}shaft\ angle)\times(body\ mass\ index)} \quad (1)$$

The rationale of the above expression is that the thickness of cortical bone is crucial for the femur to resist fracture, which has been discussed in Chapter 3. The contribution of cortical bone in resisting hip fracture is higher than that of trabecular bone as shown in the recent experimental studies [14, 75]. The results obtained by Koivumaki et al. showed that cortical bone in the proximal femur can explain 73% of the variation in the failure loads of the proximal femur during a lateral fall [14]. Nishiyama et al. suggested that the cortex of the femoral neck can carry 68.4% of the applied loads [75]. Bone mineral density is one of the most important determinants of bone strength [79]. Currently, aBMD measured by DXA is being used as a surrogate of bone strength [8, 9]. However, it has been demonstrated that aBMD cannot predict hip fracture risk accurately for all the individuals since aBMD only partly explains mechanical properties of bone [12]. Therefore, the product of CBT and aBMD is able to represent the strength of hip bone more accurately. On the other hand, positive correlations between femoral neck axis length (FNAL) and femoral neck-shaft angle (FNSA), and hip fracture risk have been found in the previous studies [58, 63-65]. These parameters in assessing hip fracture risk have been discussed in Chapter 3 in detail. Some researchers have pointed out that FNAL correlates significantly with the three types of hip fractures [61, 65] which are discussed in Section 3.1. Although individuals with larger body size have thicker CBT in the proximal femur [80], it does not mean their hip fracture risk is lower. Therefore, in order to counteract this effect and consider individual bone geometry, the product of FNAL, FNSA, and BMI is introduced. The product is expressed as a denominator in Equation (1). It is hypothesized that if a stronger correlation exists between NCBT and HFRI, NCBT can be used as the surrogate of HFRI in assessing hip fracture risk in this study.

4.2 Enrollment of Cases

Information on 210 clinical female cases, including DXA image, height, weight, aBMD and T-score were acquired from the Manitoba Bone Mineral Density Database in an anonymous way after a human research ethics approval. Since the main research objective is to investigate the correlation between NCBT and HFRI, all the cases in this study are considered as a single group. The baseline characteristics of the cases are listed in Table 4-1. The ages of the cases were between 26 and 80 years, while their heights and weights were from 57.5 to 67.9 inches and 80 to 225.4 pounds, respectively. All the cases are scanned using Lunar Prodigy DXA scanner with a standard scan mode (37.0 μGy). Scans are performed by various technicians reflecting the scenario of real clinical practices. Each DXA image is converted and saved in a MATLAB mat-file for later processing.

Table 4-1 Baseline characteristics of 210 clinical cases

Parameters	Mean (SD)
Age (years)	66.5 (8.3)
Height (in.)	62.8 (2.2)
Weight (lbs.)	140.1 (31.5)
Femoral neck BMD (g/cm^2)	0.759 (0.148)
Trochanteric BMD (g/cm^2)	0.614 (0.173)
Total hip BMD (g/cm^2)	0.783 (0.187)

4.3 Detection of the Three Critical Cross-sections on Proximal Femur

It is necessary to determine the critical cross-sections on the proximal femur prior to measuring CBT from DXA image. Usually, hip fractures occur at one of three locations on the basis of clinical observations, i.e., the narrowest femoral neck (NFN), the intertrochanter (IT) cross-section, and the femoral shaft (FS) cross-section [81]. As each DXA image is converted and saved in the MATLAB mat-file shown in Figure 4-1 using one of the studied cases, all the in-house computer codes for contour extraction, identification of relevant axes, determination of critical cross-sections, CBT measurements, and pertinent hip geometric parameters from DXA image, are developed in MATLAB.

Edge detection is performed based on the mathematical feature of DXA image, which is expressed as a matrix in MATLAB. In DXA image, the femur bone has positive pixel intensities whereas the background has negative ones. If the signs of neighbouring pixels c-

Figure 4-1 Sample of the proximal femur output from DXA image

hange from positive to negative, or vice versa, it represents the location of the boundary of the femur bone. Hence, all the boundary pixels are identified in the above way and shown as the white line in Figure 4-2.

It is much more complicated to separate the femoral head in DXA image than in CT or MRI image because the femoral head overlaps with pelvis bone resulting in the unclearness of the edge. As the femoral head can be approximated by a circle according to its shape shown in DXA image, it can be fitted by three points. Instead of picking up three points manually to define the circle, two corners indicated by two red arrows shown in Figure 4-3 are identified using the so-called corner detector [82]. The third point is the apex of the femoral head which has the minimum intensity along the femoral neck axis and it shows as the blue point in Figure 4-3. With the obtained femur contour (Figure 4-2), the NFN which is the minimum diameter of the femoral neck [69] can be located under user-defined femoral neck region; then, the femoral neck axis (FNA), which is orthogonal to the NFN and passes through the apex of the femoral head as well [64], is def-

Figure 4-2 Detected edge overlays on the proximal femur and part of the pelvis

ined and utilized to locate the apex. All the above operations are implemented using the in-house MATLAB codes. The detected NFN and FNA are shown in Figure 4-3. Until now, the outer contour of the proximal femur has been extracted and the coordinates of the contour points have been saved. The femoral shaft axis (FSA) is defined as the central line of the femoral shaft in DXA image [83], which can be obtained by a perpendicular line at the midpoint of a shaft cross-section. However, it should be pointed out that due to positioning error, the FSA may be significantly different if only a single shaft cross-section is used. Hence, a number of shaft cross-sections are selected (Figure 4-4). The midpoints of those cross-sections are utilized to define the FSA. Finally, the intertrochanter cross-section is defined as the bisector of the FNSA [69].

The three critical locations, i.e., the NFN, the IT cross-section, and the FS cross-section, are identified using the above procedure. The FS cross-section is the cross-section which has a distance of 1.5 times NFN, distal to the intersection of the neck-shaft axes [69], as shown in Figure 4-5. The femoral neck axis length (FNAL) is a modified version which

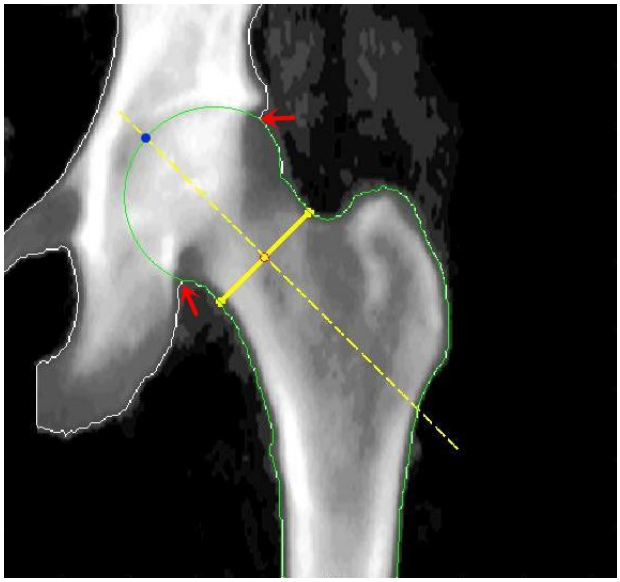

Figure 4-3 Femur contour, the narrowest femoral neck, and the femoral neck axis

is defined as a linear distance from the apex of the femoral head to the intersection of the neck-shaft axes shown as AB in Figure 4-5 in this study. Femur CBTs at the three critical cross-sections will be estimated from DXA image as described in the following section.

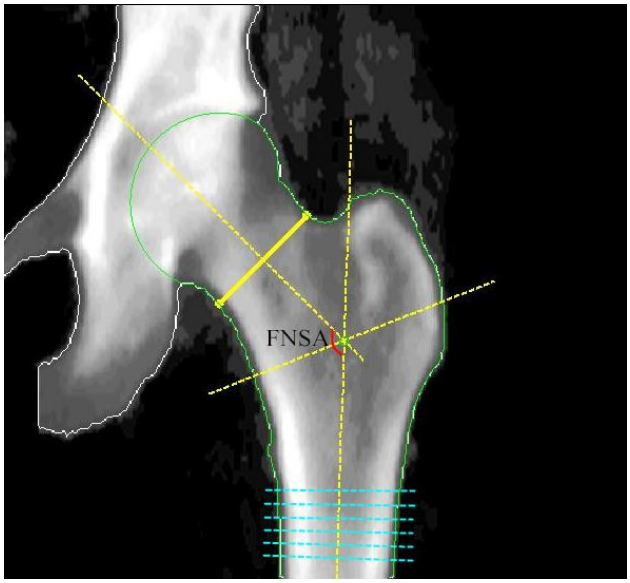

Figure 4-4 The femoral shaft axis and the bisector of FNSA. FNSA is femoral neck-shaft angle

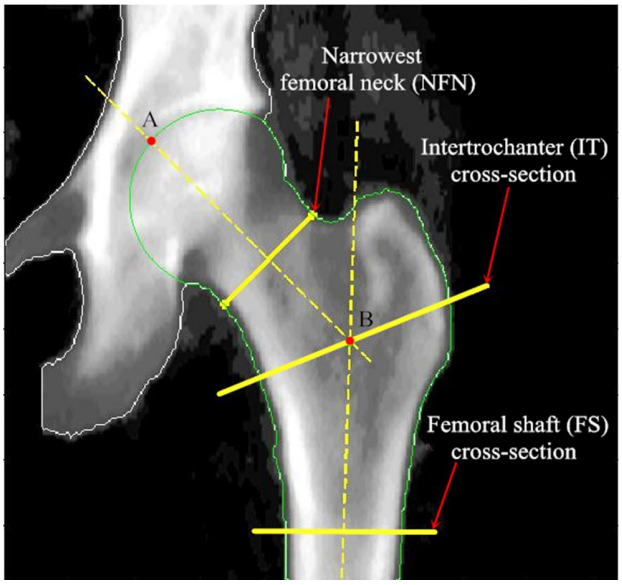

Figure 4-5 The three critical locations of hip fracture: the narrowest femoral neck (NFN), the intertrochanter (IT) cross-section and the femoral shaft (FS) cross-section. AB is the femoral neck axis length (FNAL)

4.4 Estimation of Cortical Bone Thickness from DXA Image

The idea for estimating CBT from DXA image is illustrated in Figure 4-6. The bone mass or aBMD profiles at the three critical cross-sections in a typical clinical DXA image are shown in Figure 4-6(b). The aBMD projected from the three idealized cross-sections are shown in Figure 4-6(c), which will be explained in more detail later. By comparing the aBMD profiles in Figure 4-6(b) and in Figure 4-6(c), it can be found that in each of the profile, there are existing two distinct peaks and they are exactly at the locations of the projected internal edges of cortical bone. Therefore, CBTs at the medial and lateral side of a cross-section can be determined using the starting and the ending point of the aBMD profiles together with the two distinct peaks as illustrated in Figure 4-6(c). The existence of the two distinct peaks in the aBMD profiles is not a coincidence. It is a common feature in the projection of a circular composite cross-section consisting of two material densities. The feature can be easily verified by the idealized cross-sections shown in Figure 4-6(c), where the NFN and the FS cross-section are modeled as circular annuluses, while the IT cross-section is modeled as an elliptical one [19]. The average densities (in g/cm^3) of cortical and trabecular bone at the three cross-sections are assigned respectively to the outer annulus and the inner part of the cross-sections based on the research work reported in [34]. The geometry equations of the cross-sections are written as follows:

$$\text{NFN: } \begin{cases} (x' - a)^2 + y'^2 = {r_1}^2 \\ x'^2 + y'^2 = {r_2}^2 \end{cases} \tag{2}$$

$$\text{FS: } \begin{cases} x'^2 + y'^2 = {r_3}^2 \\ x'^2 + y'^2 = {r_4}^2 \end{cases} \tag{3}$$

$$\text{IT:}\quad \begin{cases} \dfrac{(x'-A)^2}{a_1^2} + \dfrac{y'^2}{b_1^2} = 1 \\ \dfrac{x'^2}{a_2^2} + \dfrac{y'^2}{b_2^2} = 1 \end{cases} \tag{4}$$

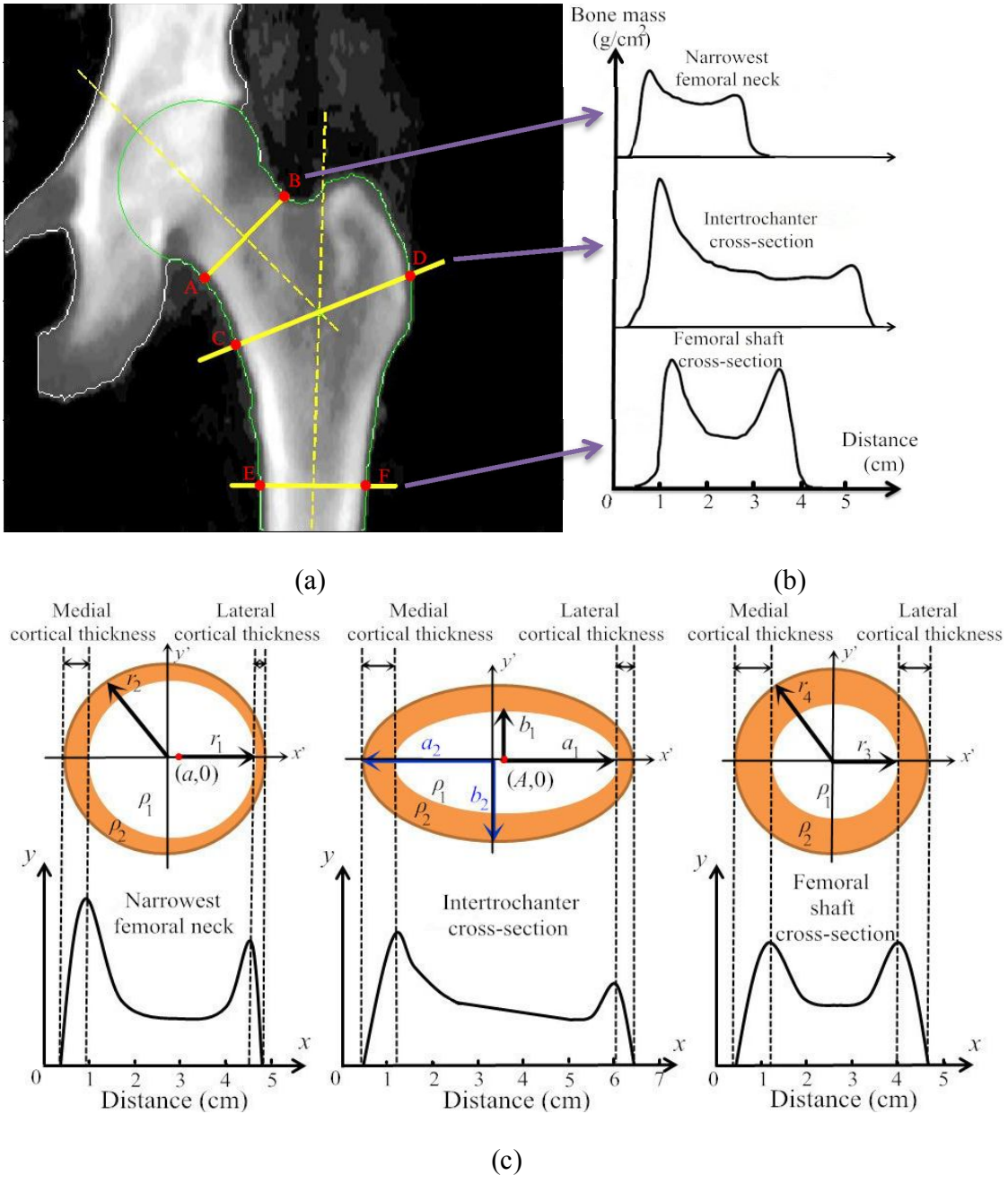

Figure 4-6 Femur CBT estimated from DXA image at the three critical cross-sections

where the meanings of geometric parameters r_1, r_2, r_3, r_4 and other items are shown in Figure 4-6(c). With the above geometry equations and the average cortical/trabecular bone densities, the projected or areal bone mineral densities (m_i, i = 1, 2…6, g/cm^2) for the three critical cross-sections can be analytically calculated as follows:

$$\text{NFN:}\quad \begin{cases} m_1 = 2[(\rho_1-\rho_2)\sqrt{{r_1}^2-(x'-a)^2} \\ \qquad +\rho_2\sqrt{{r_2}^2-x'^2}] \quad (a-r_1 \le x' \le a+r_1) \\ m_2 = 2\rho_2\sqrt{{r_2}^2-x'^2} \quad (-r_2 \le x' < a-r_1 \text{ or } a+r_1 < x' \le r_2) \end{cases} \tag{5}$$

$$\text{FS:}\quad \begin{cases} m_3 = 2\left[(\rho_1-\rho_2)\sqrt{{r_3}^2-x'^2}+\rho_2\left(\sqrt{{r_4}^2-x'^2}\right)\right] \quad (-r_3 \le x' \le r_3) \\ m_4 = 2\rho_2\sqrt{{r_4}^2-x'^2} \quad (-r_4 \le x' < -r_3 \text{ or } r_3 < x' \le r_4) \end{cases} \tag{6}$$

$$\text{IT:}\quad \begin{cases} m_5 = 2[(\rho_1-\rho_2)\sqrt{\frac{a_1^2b_1^2-b_1^2A^2+2Ab_1^2x-b_1^2x^2}{a_1^2}} \\ \qquad +\rho_2(\sqrt{{b_2}^2-\left(\frac{b_2}{a_2}\right)^2x^2})] \quad (-a_1+A \le \mathrm{x} \le a_1+A) \\ m_6 = 2\rho_2\sqrt{{b_2}^2-\left(\frac{b_2}{a_2}\right)^2x^2} \quad (-a_2 \le \mathrm{x} < -a_1+A \text{ or } a_1+A < \mathrm{x} \le a_2) \end{cases} \tag{7}$$

The three aBMD profiles in Figure 4-6(c) are plotted based on Equations (5), (6) and (7). Clearly, the existence of the two distinct peaks corresponding to the projected internal edges of cortical bone in the aBMD profiles of femur cross-sections has been verified by the idealized geometric models.

4.5 Validation with QCT-derived Cortical Bone Thickness

To validate DXA-derived CBT, QCT-derived CBT is utilized as a reference. QCT scans of forty patients (26 males and 14 females) with ages of 50-79 years (63.6 ± 8.3 years

[mean ± SD]) were obtained from the PET/CT Center at the Winnipeg Health Sciences Center in an anonymous way. The QCT sets are scanned using a standard protocol with calibration phantom. The standard protocol specifies the scan localizer starting at the anterior-posterior direction from the pelvic crest to 3-5 centimeters lower than the lesser trochanter (typically 30 cm length in total), 120 kVp, 1.5 mm slice thickness, auto exposure with a noise index of 20 HUs (Hounsfield units), 1 second scan time, pixel size of 0.09766 mm, and 512 × 512 matrix size display in helical reconstruction mode using a 50 cm scan window [84].

The obtained CT scans of the proximal femur are processed using QCT PRO software (Mindways, Texas, USA). For a set of QCT images scanned from a body part, for example the lower extremities, the software is able to automatically generates a 2-D computed tomography X-ray absorptiometry (CTXA) image, which is a DXA-like projection image (Figure 4-7). The software provides a set of utilities for operators including cortical/trabecular bone segmentation, excessive soft tissue trimming, bone hole filling, and f-

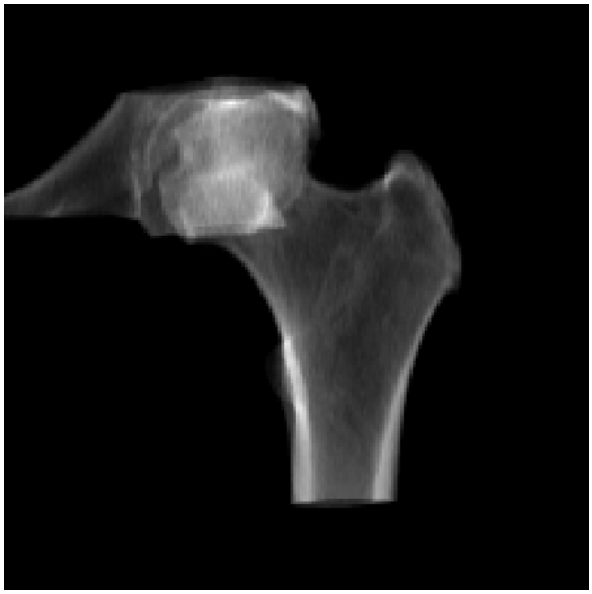

Figure 4-7 A sample CTXA image generated by the QCT PRO software

emoral neck axis adjustment, to obtain optimized DXA-like projection images. The bone investigation toolkit (BIT) included in QCT PRO is employed to do the geometry analysis of bone, including estimation of CBT. For the geometry analysis of a femur bone, the toolkit first automatically locates the three critical cross-sections as shown in Figure 4-8(a). For each of the cross-section, it is equally divided into eight sectors. An average CBT for each sector is calculated (Figure 4-8(b)). A sample bone geometry analysis report is provided in Figure 4-9, where the average cortical bone widths of the eight sectors are listed. The 3rd sector in Figure 4-9 roughly corresponds to the lateral or superior side of the proximal femur in Figure 4-8(b), while the 7th sector is approximately at the medial or inferior side of the proximal femur in Figure 4-8(b). For validation purpose, the algorithm described in Section 4.4 is used to estimate CBTs from CTXA image at the medial and the lateral side of the three critical cross-sections. The obtained results are then compared and correlated to those produced by the BIT software. Correlation studies will be performed using SPSS software. If strong correlations are found, it can be said that the in-house MATLAB codes are able to yield correct results. Average relative error denoted as $\bar{e}\,(\%)$ is introduced to compare the MATLAB-derived results and the references produced from QCT in this study:

$$\bar{e}\,(\%) = \frac{\left|Results^{(1)} - Results^{(2)}\right|}{n \times \overline{Results}} \tag{8}$$

where $Results^{(1)}$ and $Results^{(2)}$ are the results obtained by the in-house MATLAB codes and reference measurements respectively; $\overline{Results}$ is the average of them; and n is the number of the measured cases.

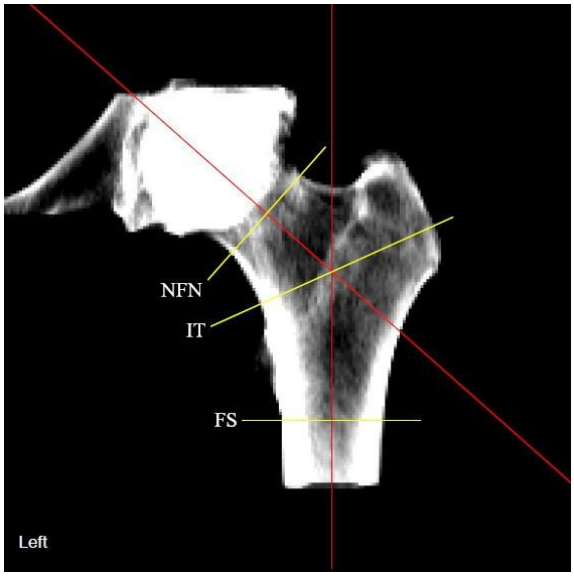

(a)

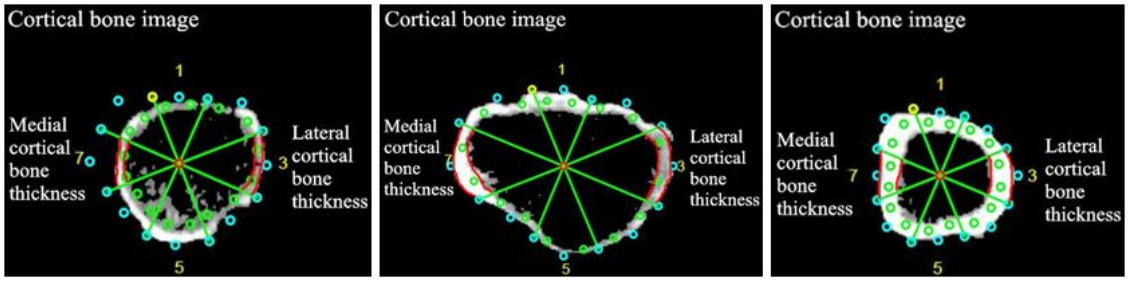

(b)

Figure 4-8 QCT-derived CBTs. (a) The three critical cross-sections from CTXA image; (b) BIT-generated CBTs in the eight sectors for the three critical cross-sections

	Perimeter	BMD	Area	Cortical Width	Norm Width	Avg Cort Arc Length	Cortical Perimeter	Distance To CM	Distance To Center	Tangent Angle	Curvature	Radius of Curvature
Sector	(cm)	(mg/cm^3)	(cm^2)	(mm)	(mm)	(mm)	(mm)	(mm)	(mm)	(degrees)	(cm^{-1})	(cm)
1	1.52	438.7	0.262	1.98	1.42	13.23	13.96	17.74	15.24	-179.4	0.109	9.20
2	1.99	483.4	0.470	2.64	2.31	17.09	18.22	20.29	19.34	-17.6	0.643	1.56
3	2.70	430.5	0.429	2.04	1.45	22.11	23.25	18.90	20.02	-81.9	0.454	2.20
4	1.86	445.8	0.594	4.49	3.24	13.64	15.87	13.61	16.16	-130.0	0.413	2.42
5	1.75	576.0	0.961	7.89	7.47	12.21	15.70	13.78	16.18	-170.2	0.818	1.22
6	2.33	512.9	0.772	4.79	4.03	15.78	18.78	12.90	13.69	140.2	0.258	3.88
7	4.72	497.1	0.417	1.43	1.17	29.22	30.59	15.41	14.18	109.6	0.356	2.81
8	5.03	543.3	0.439	1.57	1.39	34.30	35.56	17.42	14.84	48.7	0.390	2.57
Sum	21.89	3927.7	4.344	26.84	22.48	157.57	171.92	130.03	129.65	-280.4	3.439	25.86
Average	2.74	491.0	0.543	3.35	2.81	19.70	21.49	16.25	16.21	-35.1	0.430	3.23
Std Dev	1.37	52.1	0.225	2.23	2.14	8.16	7.78	2.72	2.32	124.9	0.219	2.54

Figure 4-9 Sample BIT geometry analysis report of femur bone (femoral neck)

4.6 Short-term Precision of Normalized Cortical Bone Thickness

Assessment of precision errors in the medical area is crucial as it has a great effect on the detection of longitudinal changes in the human body. Repeatability or reproducibility has been characterized by the precision errors [85]. As yet, the short-term precision of NCBT has not been investigated, and it must be studied before it can be used to predict hip fracture risk in the clinical environment, as clinical requirements are very strict to short-term precision of each of predictor. The short-term precision of HFRI should be calculated as well in order to verify its feasibility in assessing hip fracture risk based on its extent of repeatability. The calculation of HFRI will be described in Chapter 5. Total 30 paired clinical cases were selected for this investigation. Each case had an initial and a repeat scan under a standard scan mode within a few days so that the structure and property of the hip bone would not change. Short-term precision is measured by the coefficient of variation (CV), which is defined by Gluer et al. [85]:

$$CV = \sqrt{\frac{\sum_{j=1}^{n} CV_j^2}{n}} \tag{9-a}$$

$$CV_j = \frac{SD_j}{\overline{x_j}} \tag{9-b}$$

$$\overline{x_j} = \frac{x_j^{(1)} + x_j^{(2)}}{2} \tag{9-c}$$

$$SD_j = \sqrt{\frac{1}{2}\left[\left(x_j^{(1)} - \overline{x_j}\right)^2 + \left(x_j^{(2)} - \overline{x_j}\right)^2\right]} \tag{9-d}$$

where n is the number of the measured cases; $x_j^{(1)}$ and $x_j^{(2)}$ is the initial and follow-up measurement (DXA-derived CBT or HFRI) for the same subject; $\overline{x_j}$ is the mean of the measurements for this given subject j; and SD_j is the standard deviation of subject j.

Chapter 5

DXA-based Finite Element Modeling

5.1 Overview

FEA is an effective engineering approach to simulate the mechanical behavior of a complex structure. Prior to calculating stress/strain distributions, a set of pre-processing operations including generation of finite element mesh, assignment of material properties, application of loading and boundary conditions, and selection of failure criterion have to be executed. The following paragraphs will describe how to assess hip fracture risk based on the previous studies conducted by our research group using DXA-based finite element modeling [32, 33, 86].

5.2 Generation of Finite Element Mesh

The proximal femur is first segmented from DXA image before generating a FE model. This segmentation procedure has been described in Section 4.3. The boundary coordinates have been saved. One sample is plotted in Figure 5-1.

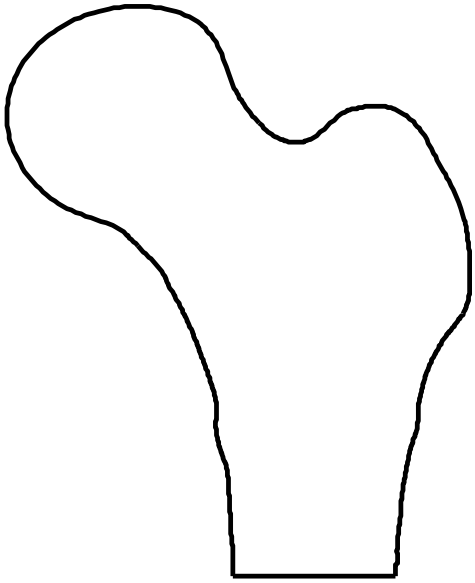

Figure 5-1 Outer contour of the proximal femur extracted from hip DXA image

As DXA image is inherently 2-D, only a 2-D finite element model can be constructed. It is assumed that the 2-D model has a uniform thickness and inhomogeneous material distribution. A plane stress model is adopted and a three-node triangle element (Figure 5-2) is selected for the finite element simulations. Although the performance of triangle elements is not as good as other types of finite elements, its simplicity is probably a practical choice for clinical applications, considering the easiness of generating a finite element mesh consisting of only triangle elements and the shorter computational time.

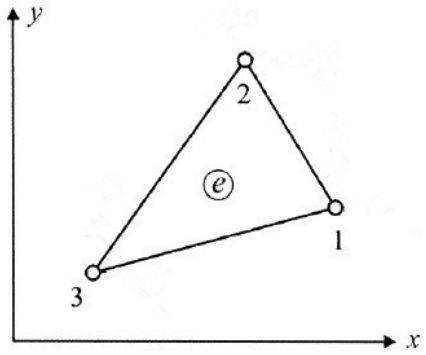

Figure 5-2 A three-node triangle element

Mesh size is a critical factor affecting the accuracy of finite element analysis. The more refined the mesh, the more accurate the results will be. However, by considering the balance between the computational cost and the accuracy requirement, a suitable mesh size should be determined based on convergence tests which will be illustrated in Section 6.1. Figure 5-3 shows a sample finite element mesh generated from the femur contour segmented from DXA image.

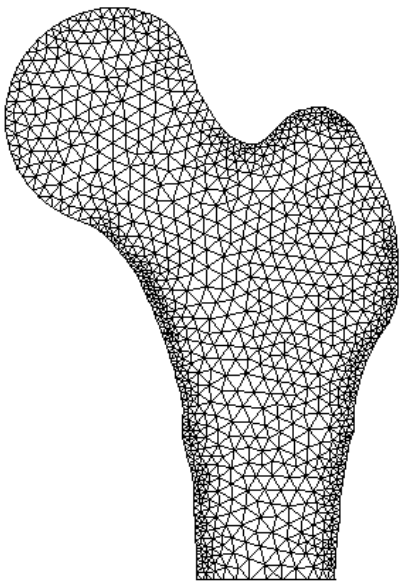

Figure 5-3 A finite element mesh generated from the femur contour segmented from DXA image

5.3 Assignment of Material Property

As described in Chapter 2, bone essentially has anisotropic and inhomogeneous material properties due to its complex microscopic architecture and composition. However, bone anisotropy information has not been captured in DXA image. It has also been demonstrated that the assignment of isotropic or anisotropic material properties only result in small differences in the final stress/strain distributions [87]. Therefore, an isotropic inhomogeneous material model is adopted to represent the proximal femur in this study.

For a plane stress problem, the material matrix $\boldsymbol{D}$ has the following format:

$$\boldsymbol{D} = \frac{E}{1-\nu^2}\begin{bmatrix} 1 & \nu & 0 \\ \nu & 1 & 0 \\ 0 & 0 & \frac{(1-\nu)}{2} \end{bmatrix} \tag{10}$$

where E is the Young's modulus of the proximal femur and υ is the Poisson's ratio. The Poisson's ratio is taken as a constant of 0.3 based on a previous study [78]. A linear correlation between pixel value and aBMD (ρ_a, in g/cm^2) has been adopted based on the previous studies [77, 86]. Young's modulus of the proximal femur is expressed by the empirical density-elasticity relationship [44, 86]:

$$E = 2838 \times \rho_a^{1.05}\ MPa \tag{11}$$

Young's modulus is assigned to element nodes based on their pixel values. All the pixels that have a pixel value larger than zero and all the element nodes are detected from DXA image. They are shown as red and blue points respectively in Figure 5-4. To determine the pixel value corresponding to an element node, a simple Euclidean distance is used to determine which pixel is the closest one to the node. Likewise, the pixel value at a Gaussian point is determined in a similar way.

By the density-pixel correlation, bone density distribution at element nodes is determined. Then, by the elasticity-density correlation, Young's modulus at element nodes and Gaussian points is determined. The latter is required in calculating the element stiffness matrix of individual elements. The global stiffness matrix is assembled from the element stiffness matrices. A sample distribution of Young's modulus is shown in Figure 5-5.

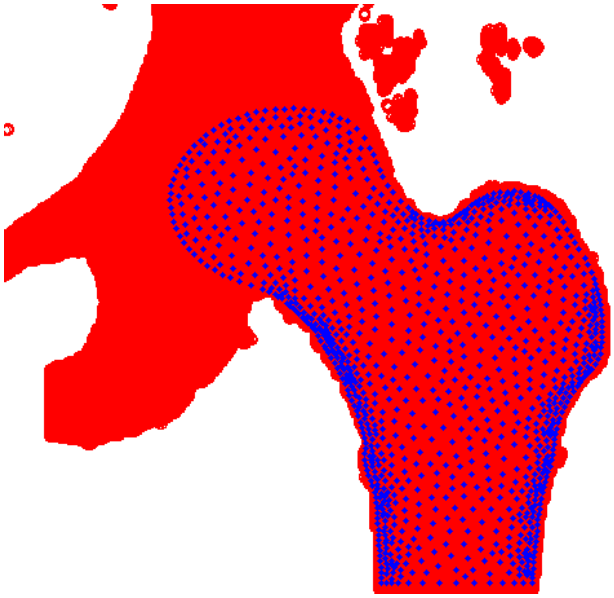

Figure 5-4 Element nodes and pixels having positive values

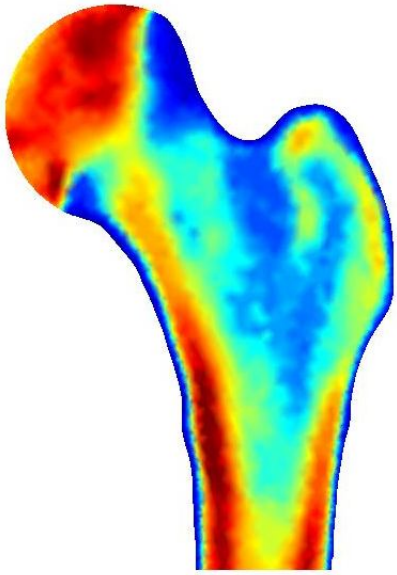

Figure 5-5 A sample distribution of Young's modulus

5.4 Application of Load and Boundary Conditions

It has been reported that more than 90% of hip fractures in the elderly are resulted from incident falls [88]. Therefore, the impact force induced in a lateral orientation and applied onto the greater trochanter is used as the loading configuration in this study. To simulate a loading condition in a sideways fall for each case, 2.5 times body weight is applied as a distributing load on the femoral head [89]. The impact force acting on the greater trochanter is given by the empirical function proposed by Robinovitch et al. [90], i.e.,

$$F = 8.25w\left(\frac{h}{170}\right)^{\frac{1}{2}} \text{ N} \tag{12}$$

where h is the height of the subject in centimeter (cm) and w is the body weight of the subject in Newton (N). The distal end of the proximal femur is completely fixed as proposed in the literature [14, 16, 75]. The load and boundary conditions simulating a sideways fall are visually shown in Figure 5-6.

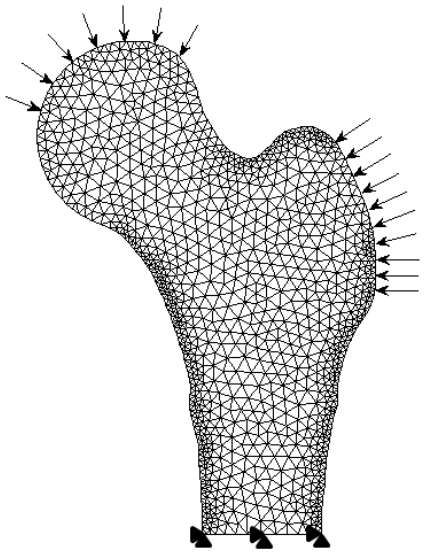

Figure 5-6 Load and boundary conditions simulating a sideways fall

5.5 Hip Fracture Risk Index Calculation at Three Regions of Interest

In order to be consistent with the clinical practice, i.e., use of average aBMD over a region of interest (ROI), and to enhance the short-term repeatability of HFRI, HFRIs over ROIs are introduced based on a previous study [32]. The locations and sizes of ROIs are taken from reference [69]. In Figure 5-7, the dashed blue lines are the central lines of the ROIs which have been defined in Section 4.3. The width of the ROIs is 10mm, which is consistent with the clinical measurement of average aBMD [69].

After defining the ROIs, selection of failure criterion should be considered. One commonly used criterion for determining material integrity in the domain of biomechanics is the von Mises criterion. This criterion states that whether the stress combination at a given point will cause failure [91]. For a plane stress model, the von Mises stress σ_{VM} is defined by the three stress components as [91]:

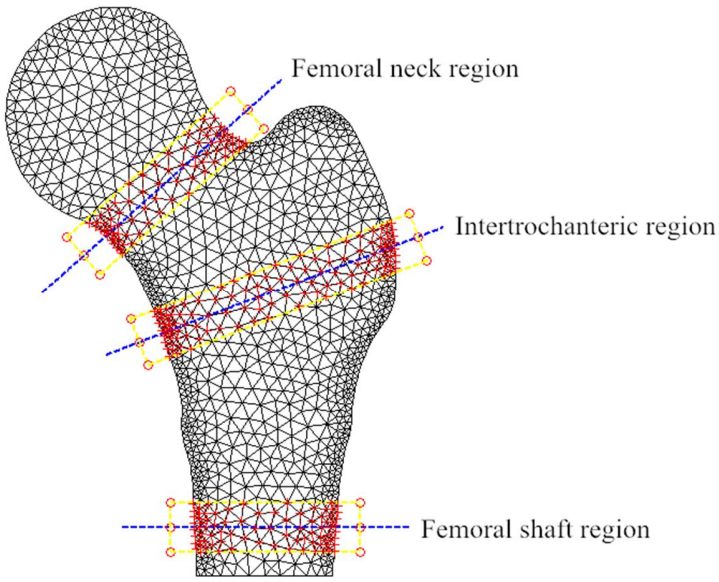

Figure 5-7 Definition of the three regions of interest

$$\sigma_{VM} = \frac{1}{\sqrt{2}} \times \sqrt{\left(\sigma_x - \sigma_y\right)^2 + \sigma_x^2 + \sigma_y^2 + 6\tau_{xy}^2} \tag{13}$$

The yield stress (σ_Y) is also correlated to aBMD (ρ_a, in g/cm^2). The empirical function in [92] is modified and adopted in our model [86]:

$$\sigma_Y = 37.4 \times \rho_a^{1.39}\ MPa \tag{14}$$

It should be noted that the strength values from Equations (11) and (14) are assigned to the corresponding Gaussian points rather than the element nodes in order to more precisely represent bone material properties. After the calculation of actual and yield stresses by the finite element analysis, HFRI over the ROI is obtained as [32]:

$$\eta_{ROI} = \frac{\sum_{i=1}^{N} \int_{A_i} \frac{\sigma_{VM}}{\sigma_Y} dA}{\sum_{i=1}^{N} A_i} \tag{15}$$

where η_{ROI} is the HFRI over an ROI such as the femoral neck region, the intertrochanteric region, the femoral shaft region, or even the whole proximal femur. A_i (i = 1, 2, …, N) are the areas of the finite elements encompassed in the specific ROI. σ_{VM} and σ_Y are the von Mises stress and the yield stress of that finite element respectively. The distribution of HFRI based on Equation (15) in a sample case is shown in Figure 5-8.

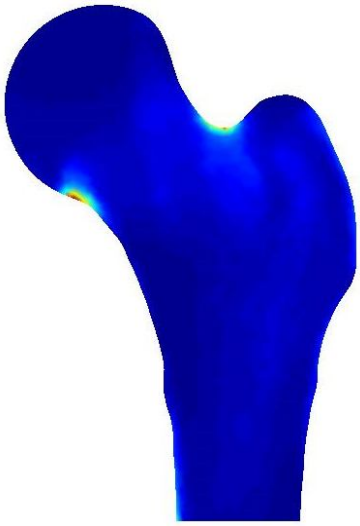

Figure 5-8 Distribution of HFRI produced by the in-house MATLAB codes

Correlations between the variables which have been introduced in Chapter 4 and this chapter will be examined by linear regression analysis using SPSS 22. Coefficients of determination r^2 are calculated. A p value < 0.05 is considered to be statistically significant. All the correlation results will be presented in Chapter 6.

5.6 Verification of the In-house Computer Codes with ANSYS Software

ANSYS (ANSYS Inc., Pennsylvania, USA) is versatile engineering simulation software which provides a simulation environment to examine a design requirement using finite element analysis. ANSYS 13.0 is thus utilized in this study to verify the in-house developed MATLAB codes which are used to construct the DXA-based finite element models. As described before, DXA image is intrinsically 2-D, so Plane 182 in the element library of ANSYS is selected. A plane stress model with a three-node triangle element with a uniform thickness and a similar mesh size is adopted in order to match the same settings of element mesh generation used in the MATLAB codes. The outer contour of the proximal femur is segmented in MATLAB. A text file containing the contour coordinates is saved and input into ANSYS. ANSYS automatically creates the element mesh over the contour using its built-in free mesh generation function. One finite element mesh sample is shown in Figure 5-9.

Ideally, the same procedure of assigning material property should have been executed in ANSYS. However, ANSYS-based temperature table which can be employed to map the inhomogeneous material properties plus the Poisson's ratio (set as a constant of 0.3 as defined in Section 5.3) only contains 100 intervals. Thereby, the scope of the Young's mod-

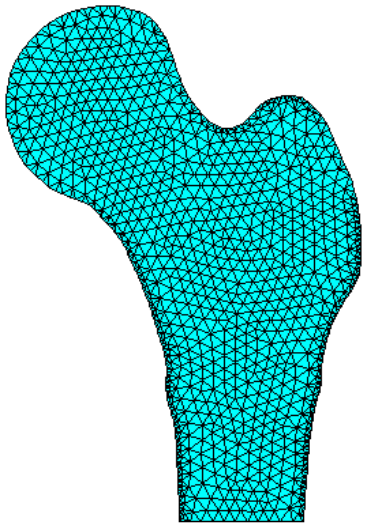

Figure 5-9 Finite element mesh generated by ANSYS

ulus can only be divided into 100 intervals in maximum. It should be emphasized that a linear interpolation is performed in ANSYS to allocate the corresponding Young's modulus to each element node using the 100 intervals defined in the temperature table. The obtained distribution of nodal Young's modulus in one case is shown in Figure 5-10(a). Meanwhile, the coordinates of the element nodes are saved in a text file; they are input into the MATLAB codes to produce the distribution of nodal Young's modulus. The obtained distribution of Young's modulus is shown in Figure 5-10(b) in order to have a visual comparison with Figure 5-10(a). Numerical comparison results will be presented in Chapter 6.

The same load and boundary conditions as in the MATLAB codes are applied to the FE model in the ANSYS simulations. One sample case is displayed in Figure 5-11. With the nodal von Mises stress produced by ANSYS simulation and the nodal yield stress computed in MATLAB, HFRIs of the three ROIs are calculated based on Equation (15). One distribution of HFRI over the proximal femur is shown in Figure 5-12.

The ANSYS-derived finite element results are then compared and correlated to those produced by MATLAB. Correlation studies will be performed using SPSS software. If strong correlations are found, it can be said that the in-house MATLAB codes can produce correct FE results. Average relative error denoted as $\bar{e}$ (%) is introduced to compare the MATLAB-derived results and the ANSYS-derived ones using Equation (8).

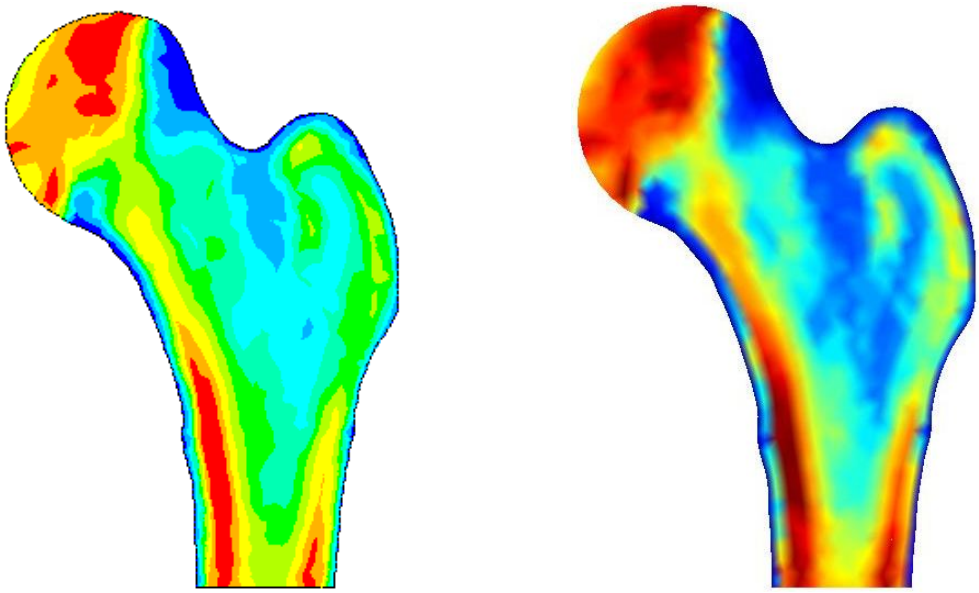

(a) (b)

Figure 5-10 Distribution of Young's modulus. (a) ANSYS-derived (b) MATLAB-derived

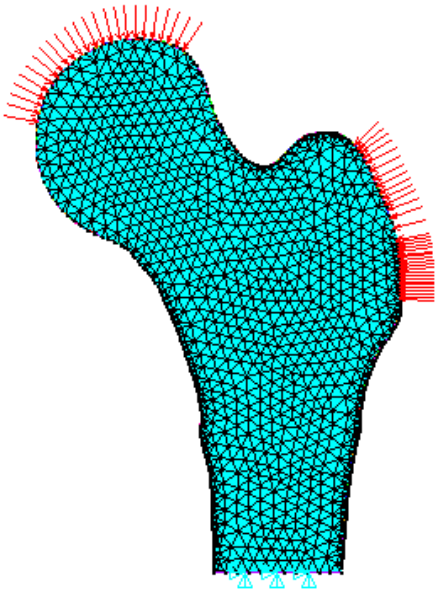

Figure 5-11 Loading and boundary conditions in ANSYS FEA

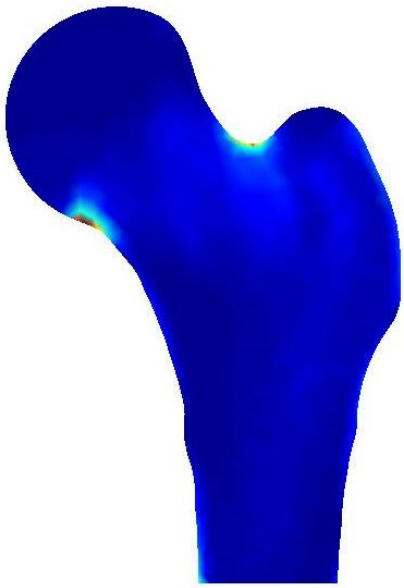

Figure 5-12 Distribution of ANSYS-derived HFRI

Chapter 6

Results

All results are reported in this chapter. Section 6.1 presents the validation results of CTXA-derived CBTs, the verification results of computer codes of DXA-based finite element modeling, and the convergence tests. Section 6.2 reports the correlation analysis results, which will justify the proposed NCBT expression. Precision study results are included in Section 6.3.

6.1 Validation and Verification Results

6.1.1 Validation of CTXA-derived Cortical Bone Thickness

The proposed algorithm for estimating CBT from CTXA (or DXA) is validated by comparing CBTs derived from CTXA with those directly obtained from QCT. Average relative errors $\bar{e}$ % between CTXA and QCT-derived CBTs are presented in Table 6-1. Correlations between CTXA and QCT-derived CBTs are presented in Figure 6-1. Figure 6-1 (a), (b), (c), (d), (e) and (f) show the correlations at, respectively, the medial (inferior) and the lateral (superior) side of the NFN, the medial and the lateral side of the IT cross-

Table 6-1 Average relative errors $\bar{e}$ (%) between CTXA and QCT-derived cortical bone thicknesses

	CTXA-QCT comparison						
	Narrowest femoral neck		Intertrochanter cross-section		Femoral shaft cross-section		Total six locations
	Medial	Lateral	Medial	Lateral	Medial	Lateral	
$\bar{e}$ %	5.76	7.95	6.18	8.13	5.03	5.74	6.51

section, the medial and the lateral side of the FS cross-section. Figure 6-1 (g) displays the correlation of all thicknesses at the six locations.

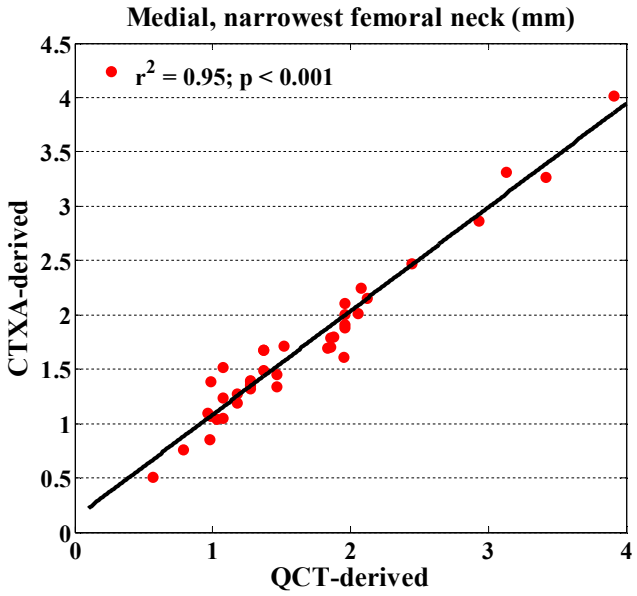

(a)

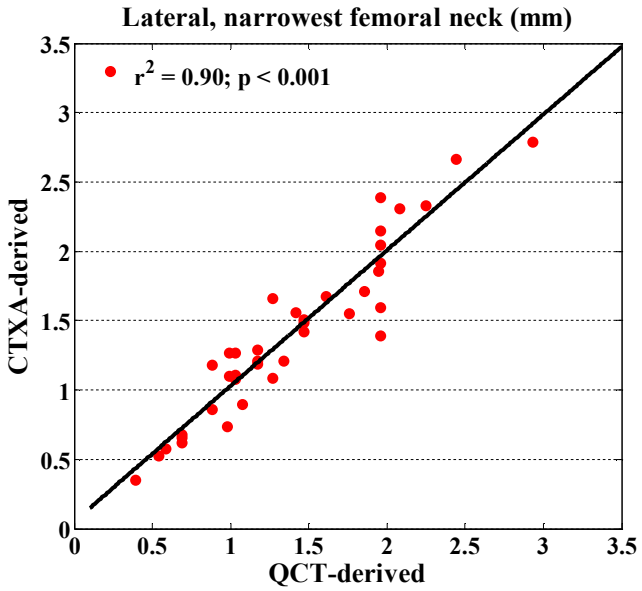
Lateral, narrowest femoral neck (mm)
r2 = 0.90; p < 0.001
CTXA-derived
QCT-derived
0
0.5
1
1.5
2
2.5
3
3.5

(b)

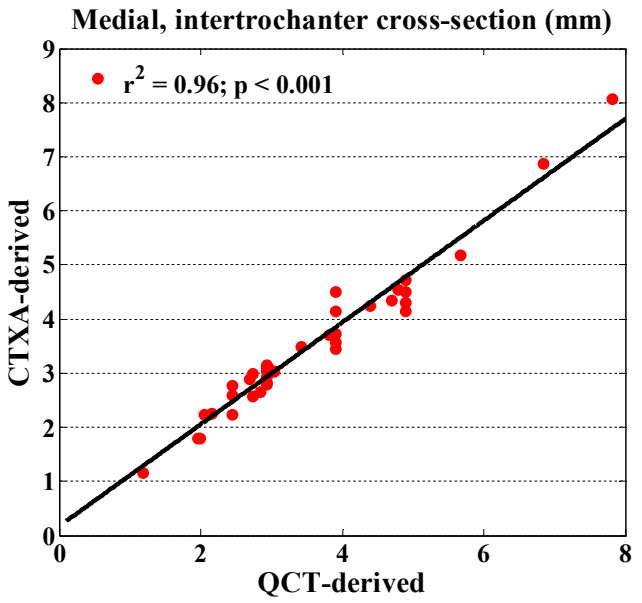
Medial, intertrochanter cross-section (mm)
r2 = 0.96; p < 0.001
CTXA-derived
QCT-derived
0
1
2
3
4
5
6
7
8
9

(c)

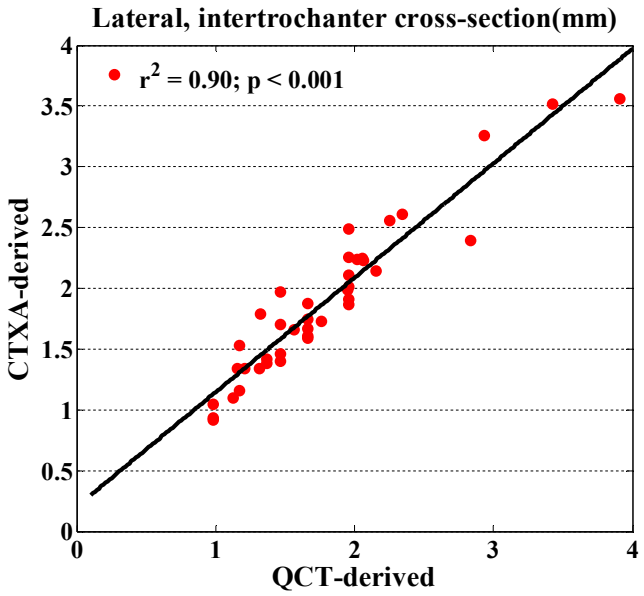
Lateral, intertrochanter cross-section(mm)
r2 = 0.90; p < 0.001
CTXA-derived
QCT-derived
0
0.5
1
1.5
2
2.5
3
3.5
4
0
1
2
3
4

(d)

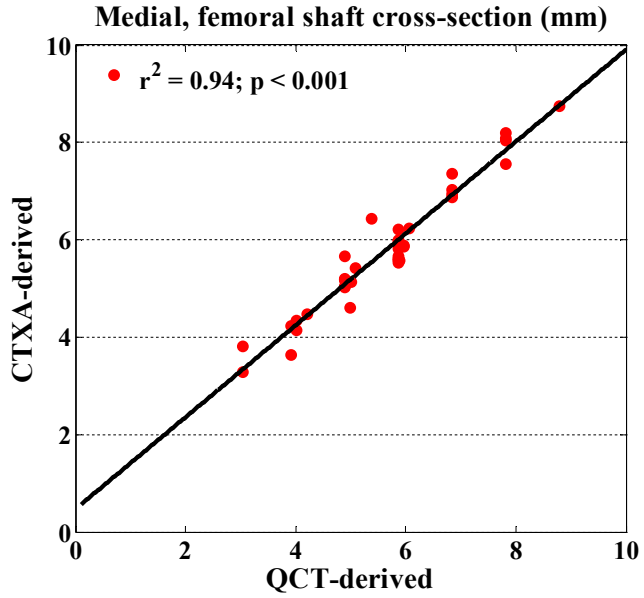
Medial, femoral shaft cross-section (mm)
r2 = 0.94; p < 0.001
CTXA-derived
QCT-derived
0
2
4
6
8
10
0
2
4
6
8
10

(e)

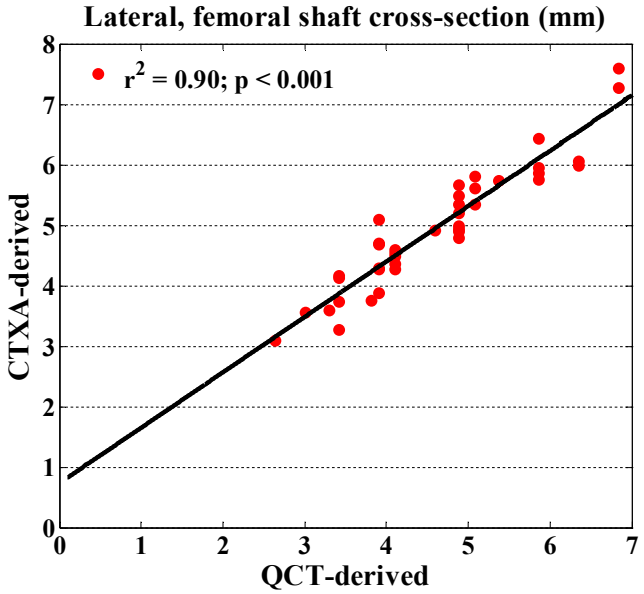

(f)

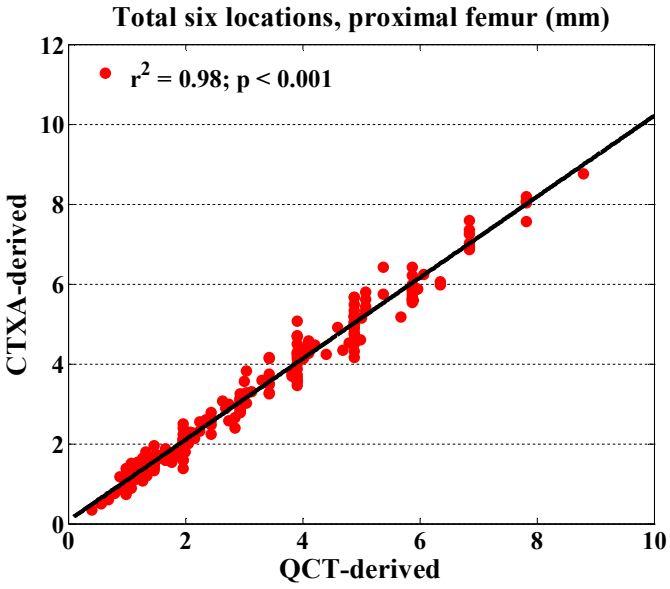

(g)

Figure 6-1 Correlations between CTXA and QCT-derived CBTs. (a) medial, narrowest femoral neck; (b) lateral, narrowest femoral neck; (c) medial, intertrochanter cross-section; (d) lateral, intertrochanter cross-section; (e) medial, femoral shaft cross-section; (f) lateral, femoral shaft cross-section; (g) all six locations

6.1.2 Verification of the Computer Codes of DXA-based Finite Element Modeling

The in-house MATLAB codes developed for DXA-based finite element modeling is verified by comparing the HFRIs produced by the in-house developed codes with those derived from the commercial software, ANSYS. Average relative errors $\bar{e}$ % between MATLAB and ANSYS-derived HFRIs are provided in Table 6-2.

Table 6-2 Average relative errors $\bar{e}$ (%) between MATLAB and ANSYS-derived hip fracture risk indices

	MATLAB-ANSYS comparison			
	Femoral neck region	Intertrochanteric region	Femoral shaft region	Total three locations
$\bar{e}$ %	6.39	6.60	7.59	6.86

Correlations between MATLAB and ANSYS-derived HFRIs are presented in Figure 6-2. Figure 6-2 (a), (b) and (c) show the correlations at the region of, respectively, the femoral neck, the intertrochanter and the femoral shaft. Figure 6-2 (d) displays the correlation for HFRIs at all the three ROIs.

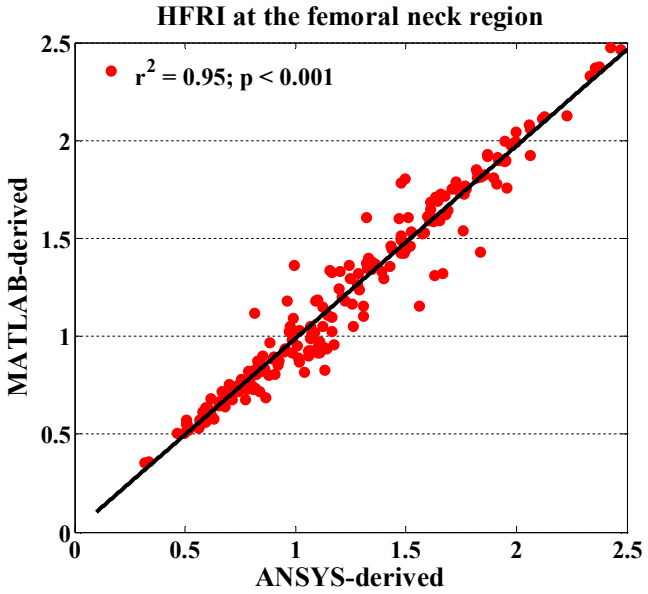

(a)

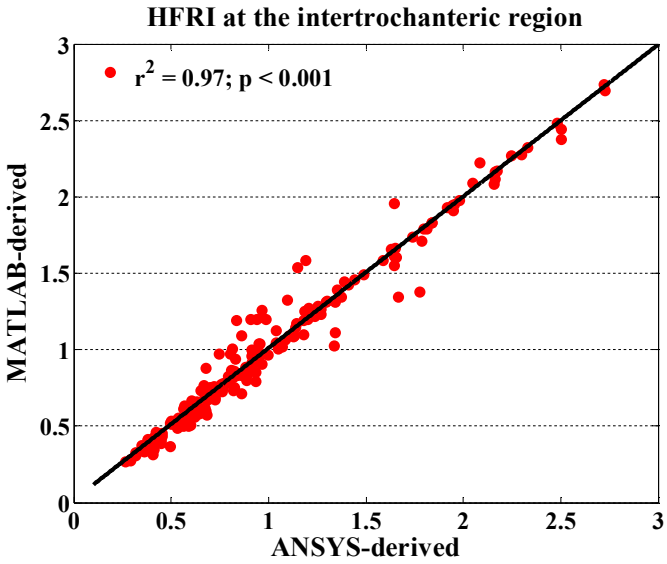
HFRI at the intertrochanteric region
r2 = 0.97; p < 0.001
MATLAB-derived
ANSYS-derived
0
0.5
1
1.5
2
2.5
3

(b)

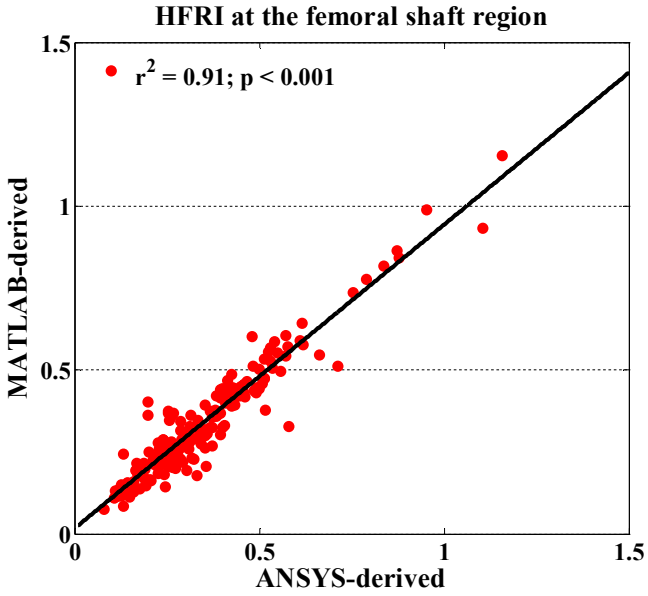
HFRI at the femoral shaft region
r2 = 0.91; p < 0.001
MATLAB-derived
ANSYS-derived
0
0.5
1
1.5

(c)

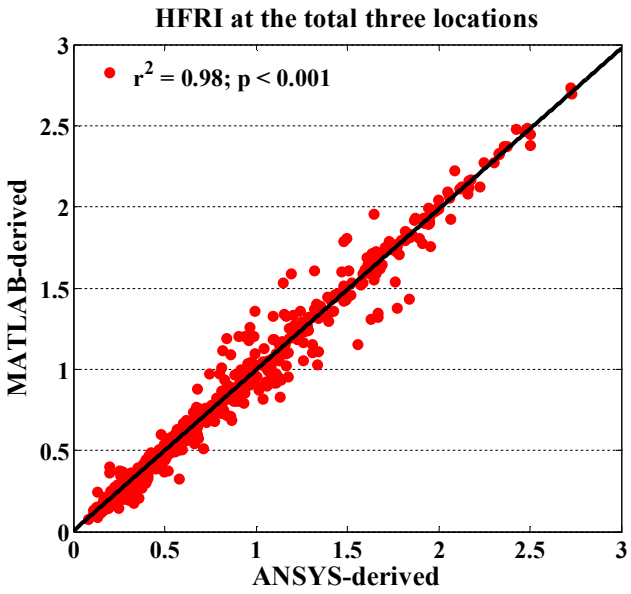

(d)

Figure 6-2 Correlations between MATLAB and ANSYS-derived HFRIs. (a) The femoral neck region; (b) the intertrochanteric region; (c) the femoral shaft region; (d) all the three ROIs

6.1.3 Convergence Tests

After verifying the in-house MATLAB codes of DXA-based finite element modeling, convergence tests were conducted to find out a mesh size that can meet both the accuracy and the computational cost requirement. For the three ROIs described in Section 5.5, the variations of the calculated HFRIs versus the number of nodes in the FE hip model are plotted in Figure 6-3.

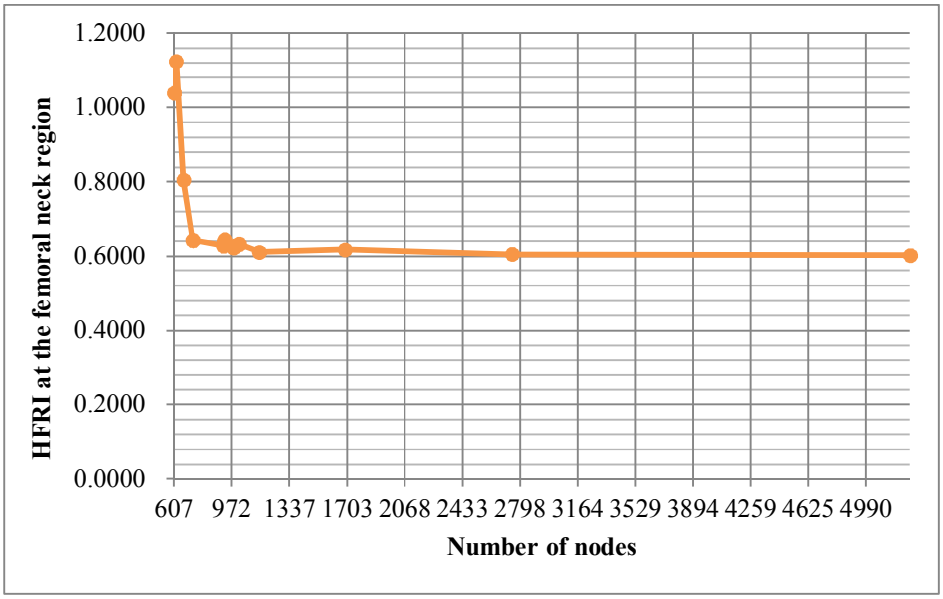
HFRI at the femoral neck region
1.2000
1.0000
0.8000
0.6000
0.4000
0.2000
0.0000
607 972 1337 1703 2068 2433 2798 3164 3529 3894 4259 4625 4990
Number of nodes

(a)

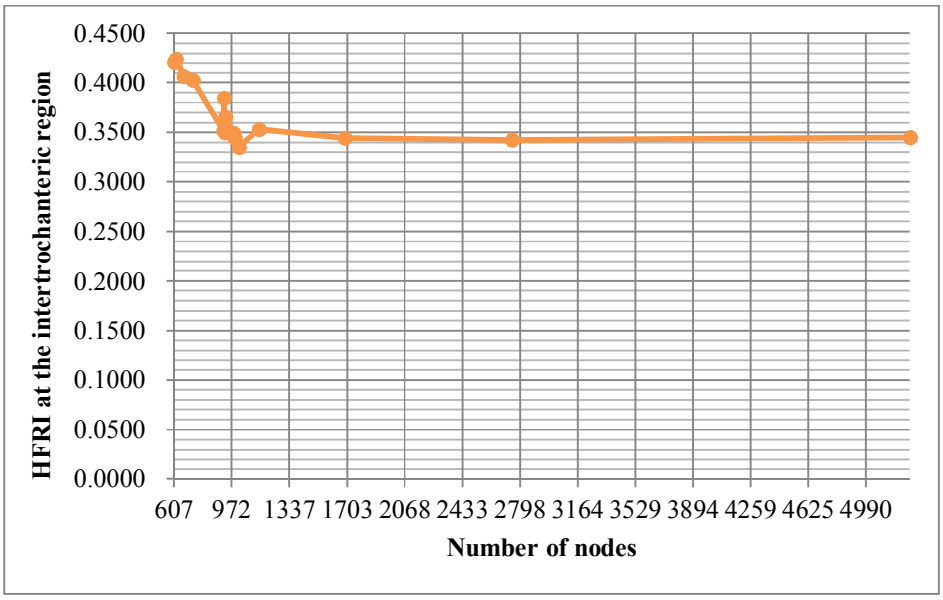
HFRI at the intertrochanteric region
0.4500
0.4000
0.3500
0.3000
0.2500
0.2000
0.1500
0.1000
0.0500
0.0000
607 972 1337 1703 2068 2433 2798 3164 3529 3894 4259 4625 4990
Number of nodes

(b)

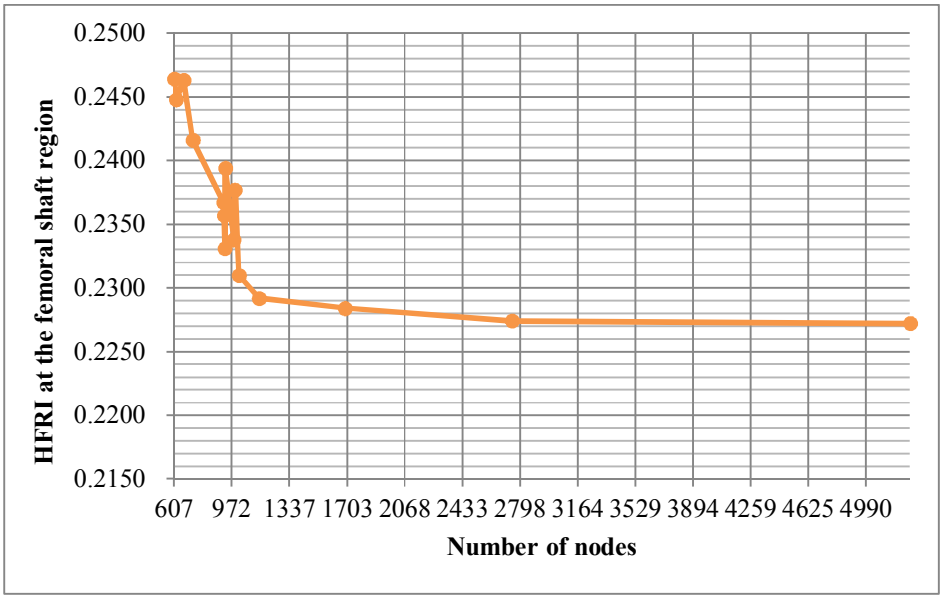

(c)

Figure 6-3 Variations of HFRIs with number of nodes at the: (a) femoral neck region, (b) intertrochanteric region, and (c) femoral shaft region

6.2 Correlation Analyses

Before showing the correlation analysis results, the means and standard deviations of DXA-derived CBTs, FNAL, and FNSA of the 210 female cases are listed in Table 6-3.

Table 6-3 Means and standard deviations of the medial and lateral cortical bone thicknesses, femoral neck axis length, and femoral neck-shaft angle in the proximal femur

Cortical bone thicknesses (mm)						Femoral neck axis length (mm) Mean (SD)	Femoral neck-shaft angle (degrees) Mean (SD)
Narrowest femoral neck Mean (SD)		Intertrochanter cross-section Mean (SD)		Femoral shaft cross-section Mean (SD)			
Medial	Lateral	Medial	Lateral	Medial	Lateral		
3.3458 (0.5199)	2.0680 (0.3733)	4.0288 (0.5104)	1.7903 (0.3528)	5.2590 (0.5582)	3.9347 (0.3835)	70.8241 (3.9233)	129.4607 (5.0810)

Correlations between HFRIs and the individual parameters included in the NCBT expression, namely, CBTs at the three critical cross-sections, aBMD, BMI, FNAL, and FNSA, are presented in Tables 6-4 to 6-6.

Table 6-4 Coefficients of determination r^2 (p value) between HFRI at the femoral neck region and individual parameters

	Femoral neck region					
	Medial CBT	Lateral CBT	aBMD	Body mass index	Femoral neck axis length	Femoral neck-shaft angle
HFRI at the femoral neck region	-0.39 (<0.001)	-0.68 (<0.001)	-0.50 (<0.001)	0.32 (<0.001)	0.37 (<0.001)	0.34 (<0.001)

Table 6-5 Coefficients of determination r^2 (p value) between HFRI at the intertrochanteric region and individual parameters

	Intertrochanteric region					
	Medial CBT	Lateral CBT	Trochanteric aBMD	Body mass index	Femoral neck axis length	Femoral neck-shaft angle
HFRI at the intertrochanteric region	-0.36 (<0.001)	-0.60 (<0.001)	-0.43 (<0.001)	0.27 (<0.001)	0.35 (<0.001)	0.28 (<0.001)

Table 6-6 Coefficients of determination r^2 (p value) between HFRI at the femoral shaft region and individual parameters

	Femoral shaft region					
	Medial CBT	Lateral CBT	Total aBMD	Body mass index	Femoral neck axis length	Femoral neck-shaft angle
HFRI at the femoral shaft region	-0.35 (<0.001)	-0.57 (<0.001)	-0.22 (<0.001)	0.25 (<0.001)	0.33 (<0.001)	0.31 (<0.001)

Correlations between femoral neck HFRI and femoral neck aBMD and T-score, and NCBT at the NFN are listed in Table 6-7. Correlations between HFRI at the intertrochanteric region and trochanteric aBMD and T-score, and NCBT at the IT cross-section are presented in Table 6-8. Table 6-9 shows the correlations between HFRI at the femoral shaft region and total aBMD and T-score, and NCBT at the FS cross-section.

Table 6-7 Coefficients of determination r^2 (p value) between femoral neck HFRI and femoral neck T-score and aBMD, and NCBT at the NFN

	NFN-Normalized cortical bone thickness		Femoral neck	
	Medial	Lateral	T-score	aBMD
HFRI at the femoral neck region	-0.63 (<0.001)	-0.81 (<0.001)	-0.50 (<0.001)	-0.50 (<0.001)

Table 6-8 Coefficients of determination r^2 (p value) between intertrochanteric HFRI and trochanteric T-score and aBMD, and NCBT at the IT cross-section

	IT-Normalized cortical bone thickness		Trochanteric	
	Medial	Lateral	T-score	aBMD
HFRI at the intertrochanteric region	-0.72 (<0.001)	-0.77 (<0.001)	-0.45 (<0.001)	-0.43 (<0.001)

Table 6-9 Coefficients of determination r^2 (p value) between femoral shaft HFRI and total T-score and aBMD, and NCBT at the FS cross-section

	FS-Normalized cortical bone thickness		Total	
	Medial	Lateral	T-score	aBMD
HFRI at the femoral shaft region	-0.60 (<0.001)	-0.67 (<0.001)	-0.21 (<0.001)	-0.22 (<0.001)

6.3 Short-term Precision Study

6.3.1 Short-term Precision of Normalized Cortical Bone Thickness

As NCBT involves CBT, FNAL and FNSA, these variables' CVs are given in Table 6-10. The CVs of NCBT are listed in Table 6-11. In order to compare with the conventional

aBMD derived from DXA scanners, CVs of average aBMD are presented in Table 6-12 as well.

Table 6-10 Coefficients of variation (CVs %) in DXA-derived cortical bone thicknesses, femoral neck axis length, and femoral neck-shaft angle

DXA-derived CBTs							
Narrowest femoral neck		Intertrochanter cross-section		Femoral shaft cross-section		Femoral neck axis length	Femoral neck-shaft angle
Medial	Lateral	Medial	Lateral	Medial	Lateral		
2.83	3.16	2.34	2.75	1.91	2.24	1.34	0.85

Table 6-11 Coefficients of variation (CVs %) in normalized cortical bone thicknesses

Normalized cortical bone thicknesses					
Narrowest femoral neck		Intertrochanter cross-section		Femoral shaft cross-section	
Medial	Lateral	Medial	Lateral	Medial	Lateral
3.27	3.41	2.59	2.85	1.93	2.38

Table 6-12 Coefficients of variation (CVs %) in average aBMD from Lunar Prodigy DXA scanners

Average aBMD		
Femoral neck	Trochanteric region	Total hip
1.22	0.85	0.64

6.3.2 Short-term Precision of Hip Fracture Risk Index

The CVs of HFRIs at the three ROIs, i.e., the femoral neck region, the intertrochanteric region, and the femoral shaft region, are provided in Table 6-13.

Table 6-13 Coefficients of variation (CVs %) in hip fracture risk indices

Hip fracture risk indices		
Femoral neck region	Intertrochanteric region	Femoral shaft region
3.10	3.94	4.16

Chapter 7

Discussion

All results presented in Chapter 6 are discussed in this chapter. Section 7.1 discusses the validation results of CTXA-derived CBTs and the verification results of the computer codes of DXA-based finite element modeling, which shows the accuracy and advantages of the in-house developed MATLAB codes, and the factors affecting the accuracy. Discussion of convergence tests is also presented. Section 7.2 discusses the correlation analysis results, which demonstrates the rationality of the proposed NCBT expression and the implications of the statistical analyses. Section 7.3 discusses the short-term precision study results of DXA-derived CBTs and computer codes of DXA-based finite element modeling, and the factors affecting the precision.

7.1 Assessment of the Validation and Verification Results

7.1.1 Assessment of the Validation Results of CTXA-derived Cortical Bone Thickness

As shown in Figure 6-1, CTXA-derived CBTs at the six locations of the proximal femur and all thicknesses at the six locations are highly correlated with QCT-derived ones (r^2 = 0.90 ~ 0.98, p <0.001), which suggests that the proposed algorithm for estimating CBT from CTXA (or DXA) image is accurate and reliable. The scope of average relative error $\bar{e}$ (%) between CTXA and QCT-derived CBTs listed in Table 6-1 is in the range of 5% ~ 8%. It has been reported that the range of accuracy of aBMD derived from DXA is about 5% ~ 10% in the clinical environment [93]. Therefore, the accuracy of the proposed algorithm for estimating CBT is within the acceptable range of clinical requirements. However, the deviations between these two measurements presented in Figure 6-1 and Table 6-1 should be discussed. One possible cause of these differences is from CBT measured by QCT. Admittedly, clinical QCT is the best tool for measuring CBT in the proximal femur. However, it generally overestimates CBT at the thinner region due to the limited resolution known as partial volume effect [94]. Partial volume effect combines two factors, namely, the limited resolution of the imaging system and the imaging sample. When limited resolution of the imaging system is used for a small object or region, it may result in an overestimate of the size of the small object or region. Therefore, this effect will overestimate the thinner regions of CBTs in the proximal femur [95]. Even the high-

resolution QCT cannot accurately measure CBTs below 1–1.5 mm [24]. As many studies have reported that CBTs at the lateral sides of the proximal femur become thinner with age [29, 73, 96, 97], the partial volume effect may result in overestimating CBTs at these sites and thus lead to larger differences as shown in Table 6-1. Although true estimates are affected by resolution in DXA as well, the proposed algorithm is still applicable for measuring CBT from DXA image, as it has been demonstrated in this study. Another source of error is that QCT PRO uses average operations to calculate medial and lateral CBT in each sector. If an improper segmentation threshold is applied to distinguish trabecular and cortical bone compartments, QCT-derived CBT may be underestimated or overestimated by the software, leading to the differences between CTXA and QCT-derived CBTs.

Apart from the influence of QCT measurement, there are two other factors affecting the accuracy of CBT measurement from CTXA or DXA image. The first one is the quality of DXA image. As described in Section 3.2.3, DXA is developed for measuring bone mineral mass rather than bone dimensions. Blur and noise are distributed over clinical DXA images. Although a de-noising procedure has been performed on DXA images in this study, the remaining noise may still bring some uncertainties into the detection of the internal and/or external edge of cortical bone, especially for patients of severe osteoporosis. Another factor is the soft tissue surrounding the proximal femur. As described in Section 4.3, the edge detection of hip contour is based on the signs of neighbouring pixels change from positive to negative, or vice versa. The femur bone has positive pixel values and some soft tissue also has positive pixel values in DXA image. This may affect the detection of the boundary of femur bone, which may regard the soft tissue as the boundary of

the femur and thus influence the identification of the starting point of cortical bone. One possible measure to solve the above issues is to implement a well-designed digital image processing algorithm to eliminate the effects of noise and soft tissue with the development of DXA technique in the future.

The proposed algorithm for estimating CBT from DXA image has several advantages. There are a few studies conducted to obtain equivalent rather than real CBT from DXA image [26-28, 70]. All the studies use the following approach to obtain equivalent CBT from DXA image based on certain assumptions. They assume simple concentric tubular models for estimating average cortical thickness. The NFN and FS cross-section are modeled as circular annuli with 40%-60% bone mineral contents of trabecular-cortical bone and 100% cortical bone respectively, while the IT cross-section is modeled as a concentric elliptical annulus which assumed 30%-70% bone mineral contents of trabecular-cortical bone. Then, the average cortical thickness for each cross-section is estimated as $w/2 - r_i$, where w is the width of each cross-section; and r_i is inner radius of each cross-section which is the function of the aforementioned constant bone mineral contents. Since it is assumed that the shapes of cross-sections are regular and the bone mineral contents are constant, the estimation cannot be accurate for individual patients. Moreover, the estimation of CBTs at the medial and the lateral side in the proximal femur cannot be done using their models. Our MATLAB codes can not only identify the three critical cross-sections of the proximal femur accurately, but also be applied to estimate medial and lateral CBT, as shown in Section 6.1.

7.1.2 Assessment of the Verification Results of the Computer Codes of DXA-based Finite Element Modeling

It can be seen from Figure 6-2 that DXA-based finite element results (HFRIs) calculated by the in-house MATLAB codes are highly correlated with ANSYS-derived ones (r^2 = 0.91 ~ 0.98, p<0.001). These high correlations verify that the in-house developed MATLAB codes of DXA-based finite element models are capable of producing correct FE results. The range of average relative error $\bar{e}$ (%) between MATLAB and ANSYS-derived HFRIs listed in Table 6-2 is from 6% ~ 8%. The differences of HFRIs computed from the in-house MATLAB codes and from ANSYS are not significant. A number of reasons may have led to the differences in the finite element results. One possible reason is the differences in finite element mesh used in the MATLAB codes and in ANSYS. A mesh generation function of three-node triangle element was developed by previous research conducted in our group [86]. In order to optimize mesh quality, especially for the irregular shape of the boundary of the proximal femur, an iterative method was implemented. In contrast, a built-in free mesh function which can be utilized to mesh a complex and irregular structure was employed in ANSYS. Because of these two different techniques in mesh construction, the calculated HFRIs may be different. Another possible reason which leads to the differences of HFRIs may be the assignment of material property. As described in Section 5.6, the temperature table in ANSYS only has 100 intervals for mapping the inhomogeneous material properties. The scope of the Young's modulus can only be divided into 100 intervals in maximum. On the other hand, the restriction does not exist in MATLAB when assigning the material properties for the proximal femur. Therefore, in the MATLAB codes, each element node and Gaussian point has its

corresponding Young's modulus derived directly from elasticity-density relationship, which will be more accurate in simulating the bone material properties than ANSYS. Therefore, the differences in material properties assignment may bring the differences into the finite element results.

The in-house developed codes for DXA-based finite element model have a number of merits for clinical applications. Compared to those existing finite element models constructed from either DXA or QCT image for evaluating femur strength [14, 16-18, 75-78], our study integrates not only subject-specific body weight in weight-bearing condition, but also individual body height in order to more accurately simulate a sideways fall. Although a few studies have reported the high correlations between experimental and finite element fracture loads using 3-D QCT-based FE models [16, 75], the benefits of high accuracy may be cancelled by the long computational time. Actually, the DXA-based subject-specific finite element model in this study only requires approximately one minute for processing with sufficient numbers of element nodes. This fast, low-cost, and relatively accurate method is convenient to provide subject-specific HFRI for clinical assessment.

7.1.3 Assessment of the Convergence Tests

Figure 6-3 shows the convergence of the MATLAB-derived HFRIs at the three ROIs of the proximal femur. Small fluctuations can be observed during the convergence processes which are mainly due to material inhomogeneity of femur bone. The FE model is completely converged at element size 5 in pixel unit. At element size 8, the obtained HFRIs at the three ROIs are only 0.4% different from the fully converged values. For a balance be-

tween accuracy and computational cost, a finite element size 8 corresponding to 2,700 ~ 2,800 element nodes should be adequate for clinical applications.

7.2 Assessment of the Correlation Analysis Results

Table 6-3 shows that compared with CBTs at the FS cross-section, CBTs at the NFN and the IT cross-section are smaller at both medial and lateral sides in this study. This is roughly consistent with the facts reported by Michelson et al. [98], i.e., 37 % and 49 % of hip fractures occur at the femoral neck and the intertrochanter separately while only 14 % are the femoral shaft fractures, as the former two cross-sections have larger volumes of trabecular bone which has much lower strength than cortical compartment [99]. The values of FNSA presented in Table 6-3 are roughly consistent with the previous studies [61, 64], whereas the values of FNAL are smaller than the previous research because of the different definition of FNAL in this study.

All the individual parameters listed in Tables 6-4 to 6-6 are significantly correlated with the corresponding HFRI. By observing the r^2 between HFRI and the individual parameters, it can be concluded that CBT, particularly at the lateral sides of the proximal femur, has dominant contributions to hip strength. The negative correlations between HFRI and the corresponding aBMD show that bone mineral density is another key factor in determining bone strength [79]. However, correlation between the total aBMD and HFRI at the femoral shaft region is relatively weaker as shown in Table 6-6. This may suggest that aBMD at the femoral shaft is more closely related to shaft strength compared to total aBMD. The positive correlations between FNAL, FNSA and the corresponding HFRI

show the proportional influences of the mentioned hip geometric parameters on hip fracture risk, which are consistent with the previous findings [63-65]. However, the positive correlation between BMI and HFRI contradicts most of the literature which considers low BMI as a risk factor for hip fracture in older women [100-102]. These studies think overweight (BMI: 25.0-29.9 kg/m^2) or obesity (BMI > 30.0 kg/m^2) has a protective effect on hip fracture because of higher BMD and cushioning effect of soft tissue during a fall [100-102]. Actually, in clinical studies, hip fracture risk is generally defined as the probability of hip fracture when considering most of the clinical risk factors in a case-control or follow-up study. However, in our FE study, only femoral aBMD, macrostructure of femur, and individual body weight and height are considered to assess hip fracture risk based on the engineering principle. Other clinical risk factors such as age, life habit, and other items cannot be included in the FE hip model. Therefore, HFRI which is defined as an average ratio between the actual stresses induced by applied forces and the allowable stresses of the femur bone over an ROI is mostly determined by the individual body weight. Moreover, 18 cases are underweight (BMI < 18.5 kg/m^2); 103 cases are normal (BMI: 18.5-24.9 kg/m^2); 51 cases are overweight (BMI: 25.0-29.9 kg/m^2); and 38 cases are obese (BMI > 30.0 kg/m^2) in this study. Since trochanteric soft tissue thickness which is important to resist hip fracture during a sideways fall [103] was not provided by the hospital and this thickness is found to be thicker in overweight or obese women than that in non-obese women, the cushioning effect of trochanteric soft tissue cannot be simulated for approximately 43% of the cases in this study. Therefore, both of the definition of HFRI and lack of damping effect of trochanteric soft tissue on the FE hip model make the positive correlation between BMI and HFRI in this study. If the buffering effect of tro-

chanteric soft tissue thickness can be incorporated in the FE loading conditions in a future study, the correlation between BMI and HFRI may be consistent with the clinical studies. Despite this contradiction, when BMI is being considered as a factor of adjusting individual differences rather than being a risk factor, it is reasonable to put it in the denominator of the NCBT expression. A recent study has shown a positive correlation between BMI and CBT in the proximal femur [80], but larger CBT in higher BMI subjects does not mean they have lower hip fracture risk, so BMI is put in the denominator in order to counteract this individual differences.

As shown in Tables 6-7 to 6-9, all NCBTs have stronger correlations with the corresponding HFRI than the aBMD and T-score. These higher correlations between NCBT and HFRI suggest that NCBT can be the substitute of HFRI in assessing hip fracture risk. In comparison with NCBTs at the medial sides of the three critical cross-sections, all the lateral sides have higher correlations with HFRIs. It can be further observed from Tables 6-7 to 6-9 that NCBT at the lateral side of the NFN is correlated most strongly with HFRI (r^2 = -0.81, p<0.001), which substantiates previous studies that local thinner part of the lateral side at the NFN may predispose a hip to fracture [29, 31, 73]. Bones generally expand with age by periosteal apposition [67], leading to more porous and thinner cortex. The process is an adaptation to maintain bone strength, as increasing the cross-section area of bone can reduce bending stress and resist bending fracture. However, if cortical bone continues to become thinner, local buckling may occur at the thinner cortex [67]. Therefore, the higher rate of bone loss at the lateral side of the proximal femur may initiate hip fractures, especially at the femoral neck, which has been reported in the previous studies [29, 31]. The maximum compressive strains occur at the lateral side of the NFN

during a sideways fall [29]. In an ex vivo experiment, cadaveric femora underwent fracture at the thin lateral cortex of the femoral neck [31].

The advantages of the proposed NCBT expression lie in considering various factors together. Considering individual differences in both body weight and height, BMI is introduced in the NCBT expression. The remaining two factors, namely, bone material property and bone geometry, are considered in the NCBT expression as well. It has been suggested that aBMD captured by DXA reflects bone material property and thus utilized in the NCBT expression. However, the key factor which leads to osteoporotic hip fractures is the reduced mechanical strength of femur in certain regions. The reduced mechanical strength of femur cannot be detected by aBMD alone. As described before, bone geometry is one of the three factors affecting the mechanical strength of bone. Therefore, structural aspects of femur are included into the NCBT expression. The combination of the above factors makes NCBT can be a surrogate of HFRI in assessing hip fracture risk in this study.

7.3 Assessment of the Short-term Precision Study Results

7.3.1 Assessment of the Short-term Precision Study Results of Normalized Cortical Bone Thickness

From Tables 6-10 to 6-12, it can be observed that DXA-derived CBTs and NCBTs are more location-sensitive than FNAL, FNSA, and average aBMD. By comparing the re-

sults listed in Tables 6-10 & 6-11, the CVs in NCBT are slightly higher than the CVs in CBT. This is reasonable as NCBT contains CBT and other hip geometric parameters which will definitely lower its repeatability. The scope of CVs in NCBT is from 2% ~ 3.5% as shown in Table 6-11, whereas for the requirement of clinical applications, the CVs should be in the range of 2% ~ 3% [85]. Hence, the repeatability of NCBT still needs to be improved before applying in the clinical environment. One main reason responsible for the lower repeatability in NCBT is that only a cross-section (line) rather than a sectional region is used in estimating CBT. By estimating CBT at a number of neighboring cross-sections and then averaging the obtained CBTs, it is possible to improve the repeatability of NCBT.

There are other factors affecting the repeatability of NCBT in this study. As discussed in Section 3.2.3, DXA is not designed for measuring spatial dimensions but bone mineral contents. Low resolution and noise in DXA image severely influence accurate edge detection of the proximal femur, particularly in the thin lateral femoral neck and/or intertrochanter. Since the detection of femur contour is crucial before estimating CBT, the intended critical cross-sections are affected by the quality of DXA image and thus lead to lower precision of NCBT. Another factor resulting in the lower precision of NCBT is the truncation of the femoral shaft in some DXA images. It affects the identification of the FSA and thus the FS cross-section. As the IT cross-section is aligned with the bisector of the femoral neck-shaft axis, the inaccurate location of the FSA affects the determination of the IT cross-section. Hence, the precision of NCBT may be affected by the hip axis placement. Finally, inconsistent positioning may be the critical factor leading to the lower precision of NCBT. If optimal precision intends to be obtained, consistency of the initial

and sequential scans must be performed on the same proximal femur. However, current quality control of DXA is only suitable for aBMD measurement. The aBMD is more tolerant to positioning error than NCBT. One of the main causations of inconsistent repositioning is hip rotation. Hip position differs by rotating around the femoral head and/or the axis of the cross-sections. Therefore, a small difference of the projecting orientation of hip has significant effects on the determinations of the three critical cross-sections as well as the estimation of CBTs. It has been reported that hip positioning devices such as jig acting at the femoral neck can considerably improve the precision of aBMD measurement [104, 105]. This may also enhance the precision of NCBT if it is applied clinically on the patients.

7.3.2 Assessment of the Short-term Precision Study Results of Hip Fracture Risk Index

It should be first noted that all HFRIs shown in Table 6-13 are obtained using the mesh size which satisfies the convergence tests. Increasing the Gauss integration order cannot considerably improve the precision of HFRI [32], so a 3-point rule is employed for all the cases when calculating HFRIs. From Table 6-13, the CVs in HFRI are in the range of 3% ~ 4%, which are generally larger than the CVs in NCBT and the average aBMD as shown in Tables 6-11 & 6-12. The lower repeatability in HFRI is normal as more factors affect the precision of HFRI than that of NCBT and average aBMD. It has been demonstrated that FEA would not introduce any random errors in the finite element modeling process if the same segmented geometric model and loading/boundary conditions are used [32]. Therefore, FEA would not introduce any differences in HFRI. However, subject position-

ing has a great effect on the precision of HFRI. Inconsistent positioning in the initial and repeat scan is the main factor to affect the precision of NCBT and aBMD as described in the previous subsection. For HFRI, this positioning error affects the projected aBMD which is utilized in the femur bone's Young's modulus and yield stress. Moreover, positioning error introduces the differences in the element mesh generation due to the discrepancy in projected geometry of the proximal femur. To improve the repeatability of HFRI, the consistency of positioning in DXA scan is required. Several procedures can be used to improve the quality of DXA scan, for example, auxiliary equipment of adjusting hip rotation can be used to keep the legs of patients have the same projected femurs; a leg-fixed device can be applied so the legs of patients would be straight and motionless during scanning.

Chapter 8

Conclusions and Future Work

Hip fracture is a global health issue. It is commonly desired to develop an improved predictor to estimate the individual hip fracture risk. In this reported research, the purpose is to find a predictor which can be used as the substitute of HFRI in assessing hip fracture risk. NCBT estimated from DXA image is then proposed. HFRI is used as a baseline for evaluating the effectiveness of NCBT in assessing hip fracture risk. In-house developed MATLAB codes for estimating CBT from DXA image and for constructing DXA-based finite element model are respectively validated and verified in this study.

8.1 Conclusions and Contributions

A total of 210 clinical female cases were obtained from the Manitoba Bone Mineral Density Database for this investigation. A novel parameter known as NCBT has been proposed in this study. It has been found that NCBTs at the six locations of the proximal femur, namely, at the medial and lateral sides of the NFN, the IT cross-section, and the FS cross-section, are highly correlated with the corresponding HFRI. Notably, NCBT at the lateral side of the NFN has the strongest correlation with HFRI at the femoral neck region

(r^2 = -0.81, p<0.001). Some procedures, such as a stricter guideline of subject positioning in DXA scanning and development of DXA technique in improving image quality, should be implemented to improve both the precision and accuracy of NCBT. This reported research suggests that NCBT can be used as the substitute of HFRI in assessing patients who are susceptible to a hip fracture in this study.

The main contributions of the current study are stated as follows:

1. An algorithm for estimating medial and lateral CBT from DXA image at the three critical cross-sections has been introduced in this study.
2. A novel predictor known as NCBT is proposed. Bone material property, bone geometry, and individual differences such as body weight and height of individual subject are considered in the NCBT expression and prove NCBT can be the substitute of HFRI in assessing hip fracture risk in this study.
3. A semi-automatic contour extraction of the proximal femur is created in this study. Individual body weight and height are incorporated into the FE model to simulate the real scenario of sideways fall instead of using a constant value.

8.2 Future Work

1. A well-defined algorithm of digital image processing will be implemented in order to eliminate the effects of noise and soft tissue surrounding the proximal femur.
2. An automatic contour extraction of the proximal femur will be developed in the future in order to eliminate the effects of manual operation.
3. An adequate and appropriately positioned region of interest will be developed in the future to replace the three critical cross-sections of the proximal femur. The means of

CBTs will be calculated on those defined ROIs in order to reduce the region sensitivity and thus improve the precision.

4. Non-linear correlations between the individual parameters and HFRIs will be considered to see how this effect affects the NCBT expression.
5. Modified version of BMI such as the ratio of fat mass or lean mass to patients' heights or specified age's heights square will be explored.
6. Sensitivity to therapy effectiveness and the ability of discriminating clinical hip fracture cases as well as fracture types will be investigated.
7. Trochanteric soft tissue thickness will be considered in the FE model.

Bibliography

[1] Browner, W. S., Pressman, A. R., Nevitt, M. C., and Cummings, S. R., 1996, "Mortality following fractures in older women: The study of osteoporotic fractures," Archives of Internal Medicine, 156(14), pp. 1521-1525.
[2] Burge, R., Dawson-Hughes, B., Solomon, D. H., Wong, J. B., King, A., and Tosteson, A., 2007, "Incidence and economic burden of osteoporosis-related fractures in the United States, 2005–2025," Journal of Bone and Mineral Research, 22(3), pp. 465-475.
[3] Melton III, L. J., 1993, "Hip fractures: A worldwide problem today and tomorrow," Bone, 14(0), pp. 1-8.
[4] Cummings, S. R., and Melton, L. J., 2002, "Epidemiology and outcomes of osteoporotic fractures," The Lancet, 359(9319), pp. 1761-1767.
[5] Hannan, E. L., Magaziner, J., Wang, J. J., Eastwood, E. A., Silberzweig, S. B., Gilbert, M., Morrison, R. S., McLaughlin, M. A., Orosz, G. M., and Siu, A. L., 2001, "Mortality and locomotion 6 months after hospitalization for hip fracture: Risk factors and risk-adjusted hospital outcomes," The Journal of the American Medical Association, 285(21), pp. 2736-2742.
[6] Salkeld, G., Cameron, I. D., Cumming, R. G., Easter, S., Seymour, J., Kurrle, S. E., Quine, S., Shanthi, N. A., and Paul, M. B., 2000, "Quality of life related to fear of falling and hip fracture in older women: a time trade off study," British Medical Journal, 320(7231), pp. 341-346.
[7] Wiktorowicz, M. E., Goeree, R., Papaioannou, A., Adachi, J. D., and Papadimitropoulos, E., 2001, "Economic implications of hip fracture: health service use, institutional care and cost in Canada," Osteoporosis International, 12(4), pp. 271-278.
[8] Kanis, J. A., and Gluer, C. C., 2000, "An update on the diagnosis and assessment of osteoporosis with densitometry," Osteoporosis International, 11(3), pp. 192-202.
[9] Kanis, J. A., Melton, L. J., Christiansen, C., Johnston, C. C., and Khaltaev, N., 1994, "The diagnosis of osteoporosis," Journal of Bone and Mineral Research, 9(8), pp. 1137-1141.
[10] Kanis, J. A., Johnell, O., Oden, A., Johansson, H., and McCloskey, E., 2008, "FRAX^{TM} and the assessment of fracture probability in men and women from the UK," Osteoporosis International, 19(4), pp. 385-397.
[11] Kanis, J. A., Oden, A., Johansson, H., Borgstrom, F., Strom, O., and McCloskey, E., 2009, "FRAX^{TM} and its applications to clinical practice," Bone, 44(5), pp. 734-743.

[12] Marshall, D., Johnell, O., and Wedel, H., 1996, "Meta-analysis of how well measures of bone mineral density predict occurrence of osteoporotic fractures," British Medical Journal, 312(7041), pp. 1254-1259.
[13] Kanis, J. A., 2008, "Assessment of osteoporosis at the primary health-care level: On behalf of the World Health Organization Scientific Group."
[14] Koivumaki, J., Thevenot, J., Pulkkinen, P., Kuhn, V., Link, T. M., Eckstein, F., and Jamsa, T., 2012, "Cortical bone finite element models in the estimation of experimentally measured failure loads in the proximal femur," Bone, 51(4), pp. 737-740.
[15] Koivumaki, J., 2013, "Biomechanical modeling of proximal femur - Development of finite element models to simulate fractures," University of Oulu, Oulu.
[16] Koivumaki, J., Thevenot, J., Pulkkinen, P., Kuhn, V., Link, T. M., Eckstein, F., and Jamsa, T., 2012, "Ct-based finite element models can be used to estimate experimentally measured failure loads in the proximal femur," Bone, 50(4), pp. 824-829.
[17] Cody, D. D., Gross, G. J., Hou, F. J., Spencer, H. J., Goldstein, S. A., and Fyhrie, D. P., 1999, "Femoral strength is better predicted by finite element models than QCT and DXA," Journal of Biomechanics, 32(10), pp. 1013-1020.
[18] Lenaerts, L., and Van-Lenthe, G. H., 2009, "Multi-level patient-specific modeling of the proximal femur. A promising tool to quantify the effect of osteoporosis treatment," Philosophical Transactions of the Royal Society, 367(1895), pp. 2079-2093.
[19] Augat, P., Reeb, H., and Claes, L. E., 1996, "Prediction of fracture load at different skeletal sites by geometric properties of the cortical shell," Journal of Bone and Mineral Research, 11(9), pp. 1356-1363.
[20] Black, D. M., Bouxsein, M. L., Marshall, L. M., Cummings, S. R., Lang, T. F., Cauley, J. A., Ensrud, K. E., Nielson, C. M., and Orwoll, E. S., 2008, "Proximal femoral structure and the prediction of hip fracture in men: A large prospective study using QCT," Journal of Bone and Mineral Research, 23(8), pp. 1326-1333.
[21] Gluer, C. C., Cummings, S. R., Pressman, A., Li, J., Gluer, K., Faulkner, K. G., Grampp, S., and Genant, H. K., 1994, "Prediction of hip fractures from pelvic radiographs: The study of osteoporotic fractures," Journal of Bone and Mineral Research, 9(5), pp. 671-677.
[22] Pulkkinen, P., Partanen, J., Jalovaara, P., and Jamsa, T., 2004, "Combination of bone mineral density and upper femur geometry improves the prediction of hip fracture," Osteoporosis International, 15(4), pp. 274-280.
[23] Hangartner, T. N., and Gilsanz, V., 1996, "Evaluation of cortical bone by computed tomography," Journal of Bone and Mineral Research, 11(10), pp. 1518-1525.
[24] Prevrhal, S., Engelke, K., and Kalender, W. A., 1999, "Accuracy limits for the determination of cortical width and density: the influence of object size and CT imaging parameters," Physics in Medicine and Biology, 44(3), pp. 751-764.
[25] Faulkner, K., and Moores, B. M., 1987, "Radiation dose and somatic risk from computed tomography," Acta Radiologica, 28(4), pp. 483-488.
[26] Kaptoge, S., Beck, T. J., Reeve, J., Stone, K. L., Hillier, T. A., Cauley, J. A., and Cummings, S. R., 2008, "Prediction of incident hip fracture risk by femur geometry variables measured by hip structural analysis in the study of osteoporotic fractures," Journal of Bone and Mineral Research, 23(12), pp. 1892-1904.

[27] Briot, K., Benhamou, C. L., and Roux, C., 2012, "Hip cortical thickness assessment in postmenopausal women with osteoporosis and strontium ranelate effect on hip geometry," Journal of Clinical Densitometry, 15(2), pp. 176-185.
[28] Beck, T. J., Looker, A. C., Ruff, C. B., Sievanen, H., and Wahner, H. W., 2000, "Structural trends in the aging femoral neck and proximal shaft: analysis of the Third National Health and Nutrition Examination Survey dual-energy X-ray absorptiometry data," Journal of Bone and Mineral Research, 15(12), pp. 2297-2304.
[29] Mayhew, P. M., Thomas, C. D., Clement, J. G., Loveridge, N., Beck, T. J., Bonfield, W., Burgoyne, C. J., and Reeve, J., 2005, "Relation between age, femoral neck cortical stability, and hip fracture risk," The Lancet, 366(9480), pp. 129-135.
[30] Poole, K. E., Mayhew, P. M., Rose, C. M., Brown, J. K., Bearcroft, P. J., Loveridge, N., and Reeve, J., 2010, "Changing structure of the femoral neck across the adult female lifespan," Journal of Bone and Mineral Research, 25(3), pp. 482-491.
[31] De-Bakker, P. M., Manske, S. L., Ebacher, V., Oxland, T. R., Cripton, P. A., and Guy, P., 2009, "During sideways falls proximal femur fractures initiate in the superolateral cortex: evidence from high-speed video of simulated fractures," Journal of Biomechanics, 42(12), pp. 1917-1925.
[32] Luo, Y., Ferdous, Z., and Leslie, W. D., 2013, "Precision study of DXA-based patient-specific finite element modeling for assessing hip fracture risk," International Journal for Numerical Methods in Biomedical Engineering, 29(5), pp. 615-629.
[33] Luo, Y., Ferdous, Z., and Leslie, W. D., 2011, "A preliminary dual-energy X-ray absorptiometry-based finite element model for assessing osteoporotic hip fracture risk," Proceedings of the Institution of Mechanical Engineers, Part H: Journal of Engineering in Medicine, 225(12), pp. 1188-1195.
[34] Yuehuei, H. A., and Robert, A. D., 2000, "Mechanical testing of bone and the bone-implant interface," CRC Press, New York.
[35] Reis, J., Silver, F. C., Queiroga, C., Lucena, S., and Potes, J., 2011, "Bone mechanotransduction: A review," Journal of Biomedical and Bioengineering, 2(1), pp. 37-44.
[36] Jee, W., 2001, "Integrated bone tissue physiology: Anatomy and physiology," Bone Mechanics Handbook, New York.
[37] Currey, J., 2002, "Bones: Structure and mechanics," Princeton University Press, Princeton, New Jersey.
[38] Blaus, B.,2013, "[Online]. Available: http://en.wikipedia.org/wiki/Long_bone."
[39] Ciarelli, M. J., Goldstein, S. A., Kuhn, J. L., Cody, D. D., and Brown, M. B., 1991, "Evaluation of orthogonal mechanical properties and density of human trabecular bone from the major metaphyseal regions with materials testing and computed tomography," Journal of Orthopaedic Research, 9(5), pp. 674-682.
[40] Silva, O. D., and Hirsch, C., 1967, "The effect of orientation on some mechanical properties of femoral cortical specimens," Acta Orthopaedica Scandinavica, 38(1), pp. 45-56.
[41] Currey, J. D., 1990, "Physical characteristics affecting the tensile failure properties of compact bone," Journal of Biomechanics, 23(8), pp. 837-844.
[42] McCalden, R. W., McGeough, J. A., Barker, M. B., and Court-Brown, C. M., 1993, "Age-related changes in the tensile properties of cortical bone. The relative importance of changes in porosity, mineralization, and microstructure," The Journal of Bone & Joint Surgery, 75(8), pp. 1193-1205.

[43] Hernandez, C. J., Beaupre, G. S., Keller, T. S., and Carter, D. R., 2001, "The influence of bone volume fraction and ash fraction on bone strength and modulus," Bone, 29(1), pp. 74-78.
[44] Morgan, E. F., Bayraktar, H. H., and Keaveny, T. M., 2003, "Trabecular bone modulus-density relationships depend on anatomic site," Journal of Biomechanics, 36(7), pp. 897-904.
[45] Johannesdottir, F., 2012, "The distribution and importance of cortical thickness in femoral neck and femoral shaft and hip fracture and lower limb fracture," University of Iceland, Vesturbar.
[46] Riggs, B. L., Khosla, S., and Melton, L. J., 1998, "A unitary model for involutional osteoporosis: Estrogen deficiency causes both Type I and Type II osteoporosis in postmenopausal women and contributes to bone loss in aging men," Journal of Bone and Mineral Research, 13(5), pp. 763-773.
[47] Lau, K. H. W., and Baylink, D. J., 1999, "Vitamin D therapy of osteoporosis: plain vitamin D therapy versus active vitamin D analog (D-hormone) therapy," Calcified Tissue International, 65(4), pp. 295-306.
[48] Guadalupe-Grau, A., Fuentes, T., Guerra, B., and Calbet, J. L., 2009, "Exercise and bone mass in adults," Sports Medicine, 39(6), pp. 439-468.
[49] 2009, "[Online]. Available: http://orthoinfo.aaos.org/topic.cfm?topic=A00392."
[50] 2000, "[Online]. Available: http://advancedortho.net/info/hipfractureinfo.php."
[51] Richmond, B., 2003, "DXA scanning to diagnose osteoporosis: Do you know what the results mean?," Cleveland Clinic Journal of Medicine, 70(4), pp. 353-360.
[52] Leib, E. S., Lewiecki, E. M., Binkley, N., and Hamdy, R. C., 2004, "Official positions of the International Society for Clinical Densitometry," Journal of Clinical Densitometry, 7(1), pp. 1-6.
[53] Adams, J. E., 2009, "Quantitative computed tomography," European Journal of Radiology, 71(3), pp. 415-424.
[54] Ho, K. Y., Hu, H. H., Keyak, J. H., Colletti, P. M., and Powers, C. M., 2013, "Measuring bone mineral density with fat–water MRI: comparison with computed tomography," Journal of Magnetic Resonance Imaging, 37(1), pp. 237-242.
[55] Bauer, J. S., and Link, T. M., 2009, "Advances in osteoporosis imaging," European Journal of Radiology, 71(3), pp. 440-449.
[56] Kanis, J. A., Johnell, O., De-Laet, C., Jonsson, B., Oden, A., and Ogelsby, A. K., 2002, "International variations in hip fracture probabilities: implications for risk assessment," Journal of Bone and Mineral Research, 17(7), pp. 1237-1244.
[57] Leslie, W. D., Lix, L. M., Johansson, H., Oden, A., McCloskey, E., and Kanis, J. A., 2010, "Independent clinical validation of a Canadian FRAX tool: Fracture prediction and model calibration," Journal of Bone and Mineral Research, 25(11), pp. 2350-2358.
[58] Leslie, W. D., Pahlavan, P. S., Tsang, J. F., and Lix, L. M., 2009, "Prediction of hip and other osteoporotic fractures from hip geometry in a large clinical cohort," Osteoporosis International, 20(10), pp. 1767-1774.
[59] Peacock, M., Turner, C. H., Liu, G., Manatunga, A. K., Timmerman, L., and Johnston, C. C. Jr., 1995, "Better discrimination of hip fracture using bone density, geometry and architecture," Osteoporosis International, 5(3), pp. 167-173.

[60] Faulkner, K., Wacker, W. K., Barden, H. S., Simonelli, C., Burke, P. K., Ragi, S., and Rio, L., 2006, "Femur strength index predicts hip fracture independent of bone density and hip axis length," Osteoporosis International, 17(4), pp. 593-599.
[61] Cheng, X. G., Lowet, G., Boonen, S., Nicholson, P. H. F., Brys, P., Nijs, J., and Dequeker, J., 1997, "Assessment of the strength of proximal femur in vitro: Relationship to femoral bone mineral density and femoral geometry," Bone, 20(3), pp. 213-218.
[62] Beck, T. J., Ruff, C. B., Scott, W. W. Jr., Plato, C. C., Tobin, J. D., and Quan, C. A., 1992, "Sex differences in geometry of the femoral neck with aging: A structural analysis of bone mineral data," Calcified Tissue International, 50(1), pp. 24-29.
[63] Bouxsein, M. L., Courtney, A. C., and Hayes, W. C., 1995, "Ultrasound and densitometry of the calcaneus correlate with the failure loads of cadaveric femurs," Calcified Tissue International, 56(2), pp. 99-103.
[64] Gnudi, S., Ripamonti, C., Gualtieri, G., and Malavolta, N., 1999, "Geometry of proximal femur in the prediction of hip fracture in osteoporotic women," The British Journal of Radiology, 72(860), pp. 729-733.
[65] Faulkner, K. G., Cummings, S. R., Black, D., Palermo, L., Gluer, C. C., and Genant, H. K., 1993, "Simple measurement of femoral geometry predicts hip fracture: The study of osteoporotic fractures," Journal of Bone and Mineral Research, 8(10), pp. 1211-1217.
[66] Stefan, U., Michael, B., and Werner, S., 2010, "Effects of three different preservation methods on the mechanical properties of human and bovine cortical bone," Bone, 47(6), pp. 1048-1053.
[67] Rivadeneira, F., Zillikens, M. C., De-Laet, C. E., Hofman, A., Uitterlinden, A. G., Beck, T. J. and Pols, H. A., 2007, "Femoral neck BMD is a strong predictor of hip fracture susceptibility in elderly men and women because it detects cortical bone instability: the Rotterdam Study," Journal of Bone and Mineral Research, 22(11), pp. 1781-1790.
[68] Beck, T. J., Ruff, C. B., Warden, K. E., Scott, W. W. Jr., and Rao, G. U., 1990, "Predicting femoral neck strength from bone mineral data: A structural approach," Investigative Radiology, 25(1), pp. 6-18.
[69] Khoo, B. C. C., Beck, T. J., Qiao, Q. H., Parakh, P., Semanick, L., Prince, R. L., Singer, K. P., and Price, R. I., 2005, "In vivo short-term precision of hip structure analysis variables in comparison with bone mineral density using paired dual-energy X-ray absorptiometry scans from multi-center clinical trials," Bone, 37(1), pp. 112-121.
[70] Beck, T. J., 2007, "Extending DXA beyond bone mineral density: Understanding hip structure analysis," Current Osteoporosis Reports, 5(2), pp. 49-55.
[71] Szulc, P., Duboeuf, F., Schott, A. M., Dargent-Molina, P., Meunier, P. J., and Delmas, P. D., 2006, "Structural determinants of hip fracture in elderly women: reanalysis of the data from the EPIDOS study," Osteoporosis International, 17(2), pp. 231-236.
[72] Holzer, G., Von-Skrbensky, G., Holzer, L. A., and Pichl, W., 2009, "Hip fractures and the contribution of cortical versus trabecular bone to femoral neck strength," Journal of Bone and Mineral Research, 24(3), pp. 468-474.
[73] Boyce, T. M., and Bloebaum, R. D., 1993, "Cortical aging differences and fracture implications for the human femoral neck," Bone, 14(5), pp. 769-778.
[74] Huiskes, R., and Chao, E. Y. S., 1983, "A survey of finite element analysis in orthopedic biomechanics: The first decade," Journal of Biomechanics, 16(6), pp. 385-409.

[75] Nishiyama, K. K., Gilchrist, S., Guy, P., Cripton, P., and Boyd, S. K., 2013, "Proximal femur bone strength estimated by a computationally fast finite element analysis in a sideways fall configuration," Journal of Biomechanics, 46(7), pp. 1231-1236.
[76] Langton, C. M., Pisharody, S., and Keyak, J. H., 2009, "Comparison of 3D finite element analysis derived stiffness and BMD to determine the failure load of the excised proximal femur," Medical Engineering & Physics, 31(6), pp. 668-672.
[77] Schileo, E., Dall'Ara, E., Taddei, F., Malandrino, A., Schotkamp, T., Baleani, M., and Viceconti, M., 2008, "An accurate estimation of bone density improves the accuracy of subject-specific finite element models," Journal of Biomechanics, 41(11), pp. 2483-2491.
[78] Testi, D., Viceconti, M., Baruffaldi, F., and Cappello, A., 1999, "Risk of fracture in elderly patients: a new predictive index based on bone mineral density and finite element analysis," Computer Methods and Programs in Biomedicine, 60(1), pp. 23-33.
[79] Martin, R. B., 1991, "Determinants of the mechanical properties of bones," Journal of Biomechanics, 24(1), pp. 79-88.
[80] Sukumar, D., Schlussel, Y., Riedt, C. S., Gordon, C., Stahl, T., and Shapses, S. A., 2011, "Obesity alters cortical and trabecular bone density and geometry in women," Osteoporosis International, 22(2), pp. 635-645.
[81] Hinton, R. Y., and Smith, G. S., 1993, "The association of age, race, and sex with the location of proximal femoral fractures in the elderly," The Journal of Bone & Joint Surgery, 75(5), pp. 752-759.
[82] Chen, H. X., and Yung, N. H. C., 2008, "Corner detector based on global and local curvature properties," Optical Engineering, 47(5), p. 057008.
[83] Van-Cauter, S., De-Beule, M., Van-Haver, A., Verdonk, P., and Verhegghe, B., 2011, "Automated extraction of the femoral shaft axis and its distal entry point from full and reduced 3D models," Taylor & Francis Group, pp. 57-61.
[84] 2013, "QCT PRO quick start guide."
[85] Gluer, C. C., Blake, G., Lu, Y., Blunt, B. A., Jergas, M., and Genant, H. K., 1995, "Accurate assessment of precision errors: How to measure the reproducibility of bone densitometry techniques," Osteoporosis International, 5(4), pp. 262-270.
[86] Ferdous, Z., 2012, "Development of a DXA–based patient-specific finite element model for assessing osteoporotic fracture risk," University of Manitoba, Manitoba.
[87] Peng, L., Bai, J., Zeng, X., and Zhou, Y., 2006, "Comparison of isotropic and orthotropic material property assignments on femoral finite element models under two loading conditions," Medical Engineering & Physics, 28(3), pp. 227-233.
[88] Grisso, J. A., Kelsey, J. L., Strom, B. L., Chiu, G. Y., Maislin, G., O'Brien, L. A., Hoffman, S., and Kaplan, F., 1991, "Risk factors for falls as a cause of hip fracture in women," The New England Journal of Medicine, 324(19), pp. 1326-1331.
[89] Yoshikawa, T., Turner, C. H., Peacock, M., Slemenda, C. W., Weaver, C. M., Teegarden, D., Markwardt, P., Blurr, D. B., 1994, "Geometric structure of the femoral neck measured using dual-energy x-ray absorptiometry," Journal of Bone and Mineral Research, 9(7), pp. 1053-1064.
[90] Robinovitch, S. N., Hayes, W. C., and McMahon, T. A., 1991, "Prediction of femoral impact forces in falls on the hip," Journal of Biomechanical Engineering, 113(4), pp. 366-374.
[91] Da-Silva, V. D., 2006, "Mechanics and Strength of Material," Springer.

[92] Kopperdahl, D. L., and Keaveny, T. M., 1998, "Yield strain behavior of trabecular bone," Journal of Biomechanics, 31(7), pp. 601-608.
[93] Blake, G. M., and Fogelman, I., 2008, "How important are BMD accuracy errors for the clinical interpretation of DXA scans?," Journal of Bone and Mineral Research, 23(4), pp. 457-462.
[94] Treece, G. M., Gee, A. H., Mayhew, P. M., and Poole, K. E., 2010, "High resolution cortical bone thickness measurement from clinical CT data," Medical Image Analysis, 14(3), pp. 276-290.
[95] Buie, H. R., Campbell, G. M., Klinck, R. J., MacNeil, J. A., and Boyd, S. K., 2007, "Automatic segmentation of cortical and trabecular compartments based on a dual threshold technique for in vivo micro-CT bone analysis," Bone, 41(4), pp. 505-515.
[96] Johannesdottir, F., Poole, K. E., Reeve, J., Siggeirsdottir, K., Aspelund, T., Mogensen, B., Jonsson, B. Y., Sigurdsson, S., Harris, T. B., Gudnason, V. G., and Sigurdsson, G., 2011, "Distribution of cortical bone in the femoral neck and hip fracture: a prospective case-control analysis of 143 incident hip fractures; the AGES-REYKJAVIK Study," Bone, 48(6), pp. 1268-1276.
[97] Bell, K. L., Loveridge, N., Power, J., Garrahan, N., Stanton, M., Lunt, M., Meggitt, B. F., and Reeve, J., 1999, "Structure of the femoral neck in hip fracture: cortical bone loss in the inferoanterior to superoposterior axis," Journal of Bone and Mineral Research, 14(1), pp. 111-119.
[98] Michelson, J. D., Myers, A., Jinnah, R., Cox, Q., and Van-Natta, M., 1995, "Epidemiology of hip fractures among the elderly: Risk factors for fracture type," Clinical Orthopaedics and Related Research, 311(0), pp. 129-135.
[99] Bayraktar, H. H., Morgan, E. F., Niebur, G. L., Morris, G. E., Wong, E. K., and Keaveny, T. M., 2004, "Comparison of the elastic and yield properties of human femoral trabecular and cortical bone tissue," Journal of Biomechanics, 37(1), pp. 27-35.
[100] Johansson, H., Kanis, J. A., Oden, A., McCloskey, E., Chapurlat, R. D., Christiansen, C., Cummings, S. R., Diez-Perez, A., Eisman, J. A., Fujiwara, S., Gluer, C. C., Goltzman, D., Hans, D., Khaw, K. T., Krieg, M. A., Kroger, H., LaCroix, A. Z., Lau, E., Leslie, W. D., Mellstrom, D., Melton III, L. J., O'Neill, T. W., Pasco, J. A., Prior, J. C., Reid, D. M., Rivadeneira, F., Van-Staa, T., Yoshimura, N., and Zillikens, M. C., 2014, "A meta-analysis of the association of fracture risk and body mass index in women," Journal of Bone and Mineral Research, 29(1), pp. 223-233.
[101] Ensrud, K. E., Lipschutz, R. C., Cauley, J. A., Seeley D., Nevitt, M. C., Scott, J., Orwoll, E. S., Genant, H. K., and Cummings, S. R., 1997, "Body size and hip fracture risk in older women: A prospective study. Study of Osteoporotic Fractures Research Group," American Journal of Medicine, 103(4), pp. 274-280.
[102] Albala, C., Yanez, M., Devoto, E., Sostin, C., Zeballos, L., and Santos, J. L., 1996, "Obesity as a protective factor for postmenopausal osteoporosis," International Journal of Obesity and Related Metabolic Disorders, 20(11), pp. 1027-1032.
[103] Majumder, S., Roychowdhury, A., and Pal, S., 2013, "Hip fracture and anthropometric variations: dominance among trochanteric soft tissue thickness, body height and body weight during sideways fall," Clinical Biomechanics, 28(9-10), pp. 1034-1040.
[104] Goh, J. C. H., Low, S. L., and Bose, K., 1995, "Effect of femoral rotation on bone mineral density measurements with dual energy X-ray absorptiometry," Calcified Tissue International, 57(5), pp. 340-343.

[105] Hans, D., Duboeuf, F., Schott, A. M., Horn, S., Avioli, L. V., Drezner, M. K., and Meunier, P. J., 1997, "Effects of a new positioner on the precision of hip bone mineral density measurements," Journal of Bone and Mineral Research, 12(8), pp. 1289-1294.